Bolstering the Rate Performance of Co-Free Ni-Rich Layered Oxide Cathode through a Rapid Heating Method

Soumyadip Mitra,[a] Thilini Rathnayaka Mudiyanselage,[b] Xijue Wang,[b] Gaurav Lohar,[c] Deepak Dubal,*[b] and Chandran Sudakar*[a]

The growing demand for high-energy density Ni-rich cathode materials, driven by the rise in lithium-ion batteries for electric vehicles and electronics necessitates fast, efficient production methods. Traditional methods for Ni-rich cathodes are energy-intensive, taking up to 24 hours, which increases costs and CO_2 emissions. In contrast, this study introduces a Co-free Ni-rich layered oxide cathode ($LiNi_{0.9}Fe_{0.05}Al_{0.05}O_2$ (NFA)) synthesis using a rapid microwave heating technique. This method takes just 2.5 hours, including heating and dwell time, while consuming minimal electricity. The microwave-annealed cathodes exhibits a well-ordered layered structure with fewer defects compared to those produced by traditional calcination (21 h). Furthermore, these cathodes display superior discharge capacities across all C-rates (e.g. 157 mAh g^{-1} at 1 C-rate and 129 mAh g^{-1} at 10 C-rate) and retain 78.1% specific capacity after 100 cycles at high current density (1 C-rate). This study paves the way for the rapid, energy-efficient synthesis of high-performance cathode materials for advanced lithium-ion batteries.

1. Introduction:

The development of clean, renewable energy sources is a global priority due to air pollution and fossil fuel scarcity. Solar, wind, and other renewables are key solutions for sustainable energy,[1] but efficient storage and rapid extraction are crucial. This has led to significant efforts to develop fast-charging batteries. Among rechargeable batteries, lithium-ion batteries (LIBs) dominate the energy storage market due to their superior electrochemical properties.[2] The demand for LIB has surged with the rise of electric vehicles (EVs) and the large-scale stationary storage. The cathode, a critical component heavily influences LIB energy density, power and cost.[3,4] While, $LiCoO_2$ cathodes have been widely used in small electronics for over 30 years, the EV industry now requires cathodes with high energy density and long cycle life. Ni-rich layered oxide cathodes ($LiNi_{1-x-y}Co_xM_yO_2$, M=Mn, Al) meet these needs with high discharge capacities (>170 mAh g^{-1}) and high energy density.[5,6] However, high nickel content (Ni≥ 0.9) leads to performance issues, such as increased cationic disorder in the crystal structure during cycling, electrolyte side reactions at highly de-lithiated state, irreversible phase transitions, the evolution of oxygen gas, and particle pulverization, which reduce their practicality for EVs.[7] These degradation pathways shorten cycle life, hindering commercialization,[8] making the development of stable Ni-rich cathodes essential for widespread use.

Researchers worldwide have various strategies to address the limitations of Ni-rich layered oxides, including cation/anion doping, surface modification, electrolyte additives, microstructural tuning, single crystalline materials, and gradient structures.[9–11] Synthesis and annealing conditions significantly influence the electrochemical properties of these cathodes.[12,13] While numerous studies examined the structural, physical, and electrochemical aspects of Ni-rich layered oxide cathodes, there is limited research on how annealing factors and the synthesis methods affect their performance.[14]

Currently, most layered oxide cathodes, synthesized via sol-gel, hydrothermal, co-precipitation, solid-state, and other techniques require prolonged high-temperature annealing (15–20 h) to achieve high crystallinity.[15] Such conventional annealing process is energy intensive and produces significant CO_2 emissions. With a projected 40-fold increase in battery material demand by 2050, reducing production cost and time is crucial. Replacing traditional furnaces with microwave (MW) heating reduces annealing time to 1–3 h, offering more energy-efficient, and environmentally friendly alternative.[16] Microwave heating ensures rapid and uniform heating, leading to high-yield, high-purity products. The main advantage is due to the microwave frequency inducing rapid and uniform heating throughout the volume of the material.[17] While microwave annealing has been explored for Li and Na ion battery electrodes,[18–20] there are no reports on using it for Ni-rich layered oxides with over 80% Ni concentration.

In addition to reducing synthesis time, selecting right transition metal (TM) is essential. Currently Ni-rich cathodes, such as NMC and NCA, use Mn, Co, and Al in varying ratios.[21] While Co lowers cationic disorder and improves rate perform-

[a] S. Mitra, C. Sudakar
Multifunctional Materials Laboratory, Department of Physics, Indian Institute of Technology Madras, Chennai-600036, India
Telephone: +91-44-2257-4895
E-mail: csudakar@iitm.ac.in

[b] T. Rathnayaka Mudiyanselage, X. Wang, D. Dubal
Centre for Materials Science, School of Chemistry and Physics, Queensland University of Technology, Brisbane, QLD 4000, Australia
E-mail: deepak.dubal@qut.edu.au

[c] G. Lohar
Department of Physics, Lal Bahadur Shastri College of Arts, Science and Commerce, Satara-415002, India

Supporting information for this article is available on the WWW under https://doi.org/10.1002/batt.202400782

Batteries & Supercaps

Research Article
doi.org/10.1002/batt.202400782

Chemistry Europe
European Chemical
Societies Publishing

ance, its high costs, limited availability, toxicity, and purification challenges hinder its use in EV batteries.[22,23] Consequently, there is a growing interest in eliminating or reducing the cobalt content.[24] Nevertheless, the ternary layered oxide's avoiding Co compromises the crystal structure's stability, and hence an appropriate alternate approach is required to address the issue.[25] Iron, with a similar ionic radius to Ni^{3+} ($r(Fe^{3+}) = 0.55$ Å and $r(Ni^{3+}) = 0.56$ Å), is a promising substitute for Co, as it stabilizes the crystal structure and improves the cycle life.[26,27] Some studies have explored Fe-substituted, Co-free Ni-rich layered oxide cathode by utilizing sol-gel, co-precipitation, and rheological phase reaction methods.[28–30]

In this work, Co-free $LiNi_{0.9}Fe_{0.05}Al_{0.05}O_2$ (NFA) cathode is synthesized using precursors obtained from the solvothermal method and processed under the optimized annealing conditions using both the conventional and microwave annealing methods. Unlike the traditional annealing, which requires 15–20 h of high-temperature heating, microwave annealing speeds up the process, producing high-quality Ni-rich layered oxide cathodes in just 2–3 h. This study discusses the effects of conventional and microwave annealing on the crystal structure, morphology, high-rate capability, and long-term cycling stability of Co-free $LiNi_{0.9}Fe_{0.05}Al_{0.05}O_2$ (NFA) cathodes. By enhancing reaction speed, reducing energy consumption, and improving product quality, MW annealing offers significant advantages, including high-rate capability, discharge capacity and cyclic stability, compared to conventional annealing. This makes it a more environmentally friendly and sustainable approach for Ni-rich layered oxide cathode production.

Experimental Section

Ni-rich layered oxide with the composition $LiNi_{0.9}Fe_{0.05}Al_{0.05}O_2$ (NFA) has been prepared by employing two different annealing method: (i) Conventional annealing and (ii) Microwave annealing. The specifics of each of these methods are provided below.

Synthesis of NFA Cathode

Utilizing isopropyl alcohol (Sigma-Aldrich; IPA) as the solvent, the hydroxide precursor for the $LiNi_{0.9}Fe_{0.05}Al_{0.05}O_2$ (NFA) cathode is synthesized by a solvothermal method. The inorganic precursor solution was made by dissolving the salts of $Ni(NO_3)_2.6H_2O$ (99%; Merck), $Fe(NO_3)_2.6H_2O$ (98%; Merck), and $Al(NO_3)_3.4H_2O$ (98.5%; Merck) in 60 ml of IPA solution in the required stoichiometric ratio, i.e., Ni: Fe: Al = 0.9:0.05:0.05 based on the formula $LiNi_{0.9}Fe_{0.05}Al_{0.05}O_2$. At room temperature, the mixture is vigorously stirred continuously for 1 h. The metal salt solution was then transferred to a 100 ml Teflon-lined stainless-steel autoclave and heated to 180 °C for 12 h in a hot air oven. The precursor is then filtered and repeatedly cleaned with absolute ethanol several times. The cleaned precipitate was subsequently dried for 12 h at 70 °C in a vacuum oven (10 mbar). After the dried metal hydroxide precipitate was thoroughly mixed in an agate mortar for about 30 min with a stoichiometric amount of $LiOH.H_2O$ (Alfa Aeser; 5% excess is added to compensate the Li loss at high-temperature annealing), the mixed powder was preheated to 480 °C in a tubular furnace for 5 h in a high pure oxygen ambient (99.999%) by setting a heating rate of 2 °C/min.

Finally, the pre-heated powder is MW annealed at 800 °C for different holding times of 15 min, 30 min, 45 min, and 60 min. The average heating rate to reach the final set temperature during the annealing process is ~6 to 7 °C/min. The samples were also annealed at lower temperatures (700 °C and 750 °C), however, they lead to poorly ordered layered structure and hence poor electrochemical performance. After the MW irradiation, the samples are allowed to cool to room temperature in the furnace and kept inside the argon-filled glove box for further characterization. The samples obtained via different annealing times are labelled as NFA-15, NFA-30, NFA-45, and NFA-60. After pre-annealing at 480 °C, the NFA cathode obtained from the solvothermal process is also prepared by annealing in a traditional tubular furnace. The pre-annealed precursor was calcined at 800 °C for 15 h with a heating rate of 5 °C/min. The sample is labelled as NFA-CONV.

Material Characterization

The X-ray diffraction data of all the samples are collected using a Rigaku SmartLab Diffractometer having a Cu–K_α radiation ($\lambda = 0.15406$ nm) in the range of 10°-80° (2θ). Raman spectra of all the samples are obtained using Raman microscope using an excitation wavelength of 632 nm from a He–Ne laser source. A diffraction grating of 1800 lines/cm is used to disperse the scattered light during the measurement. The field emission scanning electron microscope (FESEM) using Inspect F50 (FEI) is employed to examine the surface morphology of all the layered oxide cathodes. The same microscope is used to determine the elemental composition and the elemental mapping using the energy-dispersive X-ray spectroscopy (EDS) mode with an operating voltage of 20 kV. X-ray photoelectron spectroscopy (Kratos AXIS supra spectrometer) measurements are performed to determine the surface valence state of all both the samples.

Electrochemical Characterization

The electrochemical performance of all the synthesized cathodes is studied using CR2032 coin cells in the half-cell configuration. The electrodes are created by mixing the active materials (NFA-CONV, NFA-15, NFA-30, NFA-45, and NFA-60), conductive carbon black, and PVDF binders (8:1:1 in weight) in N-methyl-2-pyrrolidone (NMP) to obtain the cathode slurry. The homogeneously mixed slurry is coated (thickness 100 μm) on aluminum foil and subsequently dried in a vacuum oven at 80 °C for 12 h (~10 mbar) to remove the NMP solvent. The dried foils were punched into circular pieces of 12 mm diameter. The mass loading on all the cathode foils (NFA-15, NFA-30, NFA-45, and NFA-60) is in the range of 1.1–1.2 mg. The coin cells are assembled in an argon-filled glove box with active material coated circular foils as cathode, lithium metal as a counter electrode, and a glass microfiber as a separator. 1 M $LiPF_6$ dissolved in a solvent mixture of ethylene carbonate (EC), dimethyl carbonate (DMC), and diethyl carbonate (DEC), in a ratio of 1:1:1 (vol %) is employed as an electrolyte solution. Charge-discharge tests were executed at constant currents ranging from 20 to 5000 mA/g (≡ 0.1 C to 25 C) in the voltage window of 2.8 to 4.5 V (versus Li/Li⁺). The testing was carried out using Neware battery testers at room temperature. The cyclic voltammetry measurements are carried out to obtain the diffusion coefficients of all the cathode materials at room temperature in the voltage range of 3.0–4.5 V in a Biologic VSP electrochemical workstation. In the same workstation, Galvanostatic intermittent titration technique (GITT) is carried out to determine the Li-ion diffusion coefficient as a function of potential at 0.1 C-rate. The measurement was performed by applying a current pulse for 20 min followed by a relaxation period for 2 h.

Batteries & Supercaps

Research Article
doi.org/10.1002/batt.202400782

Chemistry Europe
European Chemical
Societies Publishing

2. Results and Discussion

2.1. Principle of MW Heating Mechanism

The process by which microwave (MW) heating functions differs significantly from that of conventional heating. Unlike conventional heating, which relies on conduction, convection, or radiation to transfer heat, MW heating uses electromagnetic radiation in the MW frequency range to deliver energy directly to the molecules of a substance. This electromagnetic radiation consists of electric and magnetic fields oscillating at the microwave frequency. One key feature of MW heating is its "inside-to-surface" heating mechanism, in which the material's molecules absorb the MW radiation, resulting in rapid and uniform heating throughout the material's entire volume. This uniform heating minimizes temperature gradient both within and between particles, ensuring consistent and effective heating. Conversely, conventional heating follows a "surface-to-inside" process, where heat is transferred from the material's outer surface inward via conduction. This results in slower and less uniform heat distribution. To ensure that all particles reach the required temperature, such a slow and uneven heat conduction system necessitates longer heating times, particularly during high-temperature annealing.

2.2. Structural Studies

The phase identification and the crystallographic information of all the cathodes are studied using XRD. The XRD pattern of the pre-annealed $LiNi_{0.9}Fe_{0.05}Al_{0.05}O_2$ precursor powder is shown in Figure S1 (see the Supplementary Information). The pattern confirms the initial construction of the rhombohedral structure of NiO, as evidenced by the diffraction peaks of (003), (012), and (104)/(110). The pattern also includes anhydrous LiOH peaks, indicating an incomplete reaction of LiOH with pre-annealed oxide precursor at 480 °C. Figure 1 presents the XRD patterns obtained from all the NFA cathodes. This picture also includes the ICSD data (ICSD # 98-005-9191)[31] from a standard $LiNiO_2$ composition. The Xpert high score plus software is used to carry out the Rietveld refinement of each sample and the corresponding refined patterns are presented in Figure S2. The sharp diffraction peaks from all the samples substantiate good crystallinity in all the cathodes. The sample treated at 800 °C for 15 h in a conventional tube furnace (NFA-CONV) showed a α-$NaFeO_2$ hexagonal lattice with the $R\bar{3}m$ space group. The presence of minor impurity peaks at ~35° and ~58° can be correlated with the presence of Li_2O peaks of $Fm\bar{3}m$ space group[32] . It is well known that the (003) peak's intensity always exceeds that of the (104) peak in a well-ordered layered structure with less cationic disorder.[33] In general, a high degree of Ni^{2+} ions in the Li–O layer (severe cation mixing) of the layered structure is indicated by an I(003)/I(104) intensity ratio
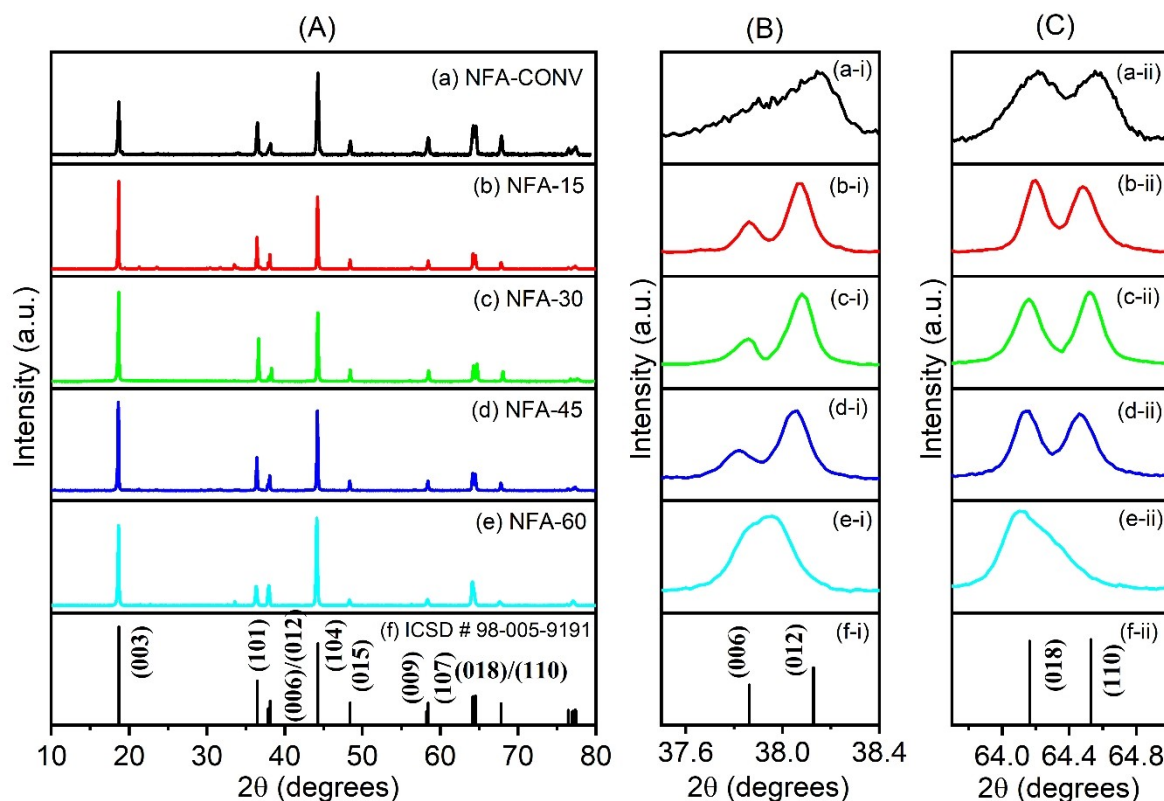
Figure 1. X-ray diffraction patterns of Ni-rich layered oxides. (Panel A): (a) NFA-CONV, (b) NFA-15, (c) NFA-30, (d) NFA-45, and (e) NFA-60 cathodes. (f) Standard ICSD data (ICSD # 98–005-9191) of hexagonal Ni-rich layered oxide phase. Panel B is magnified regions of the XRD pattern for the peaks (006)/(012). Panel C is the magnified regions of the XRD pattern for the peaks (018)/(110).

Batteries & Supercaps

Research Article
doi.org/10.1002/batt.202400782

Chemistry Europe
European Chemical
Societies Publishing

of less than 1.2. Additionally, this promotes the structural change from a hexagonal to a cubic system.[34] The integrated intensity ratio of (003) and (104) peak is well below 1 for NFA-CONV cathode suggesting a higher degree of cationic disorder in the layered structure. According to published reports, a well-ordered hexagonal layered structure can be identified by the distinct splitting of diffraction peaks (006) and (012) at $2\theta \approx 38°$ and (018) and (110) at $2\theta \approx 65°$.[35] It should be noted that the splitting of (006)/(012) and (018)/(110) pairs are unclear (Figure 1B (a–i) and Figure 1C (a-ii)) in the case of NFA-CONV cathode suggesting a significant cation mixing and poorly ordered layered structure. The XRD pattern of the NFA-15 cathode shows the formation of the hexagonal layered structure of Ni-rich layered oxide with the $R\bar{3}m$ space group. Additionally, arrow-designated contaminants were visible in the sample (Figure S2 (b)). These contaminants result from the presence of impurity peaks. A peak at approximately 21.2° and 31° can be identified as Li_2CO_3 phase, whereas the existence of impurity peak at approximately 35° can be associated with the presence of Li_2O peak. Extending the MW reaction time to 30 min completes the formation of α-$NaFeO_2$ hexagonal lattice type structure without any impurities suggesting the formation of phase pure Ni-rich layered oxide in NFA-30 cathode. Interestingly, the intensity ratio of the (003) peak is larger than that of the (104) peak (more than 1.2), suggesting that annealing the cathodes by MW treatment have less cationic disorder. The integrated intensity ratio of (003) and (104) planes was found to be around 1.22, and 1.29 for NFA-15, and NFA-30 samples, respectively. I(003)/I(104) intensity ratio of more than 1.2 is the result of the MW annealing's short ramping and reaction times, which provide little time for substantial cation mixing. The clear splitting of (006)/(102) and (018)/(110) pairs (Figure 1B (b–i)–(c–i) and Figure 1C (b–ii)–(c–ii)) further substantiates the creation of well-ordered O3-type layered structure with reduced cationic disorder for NFA-15 and NFA-30 cathode. The NFA-45 cathode demonstrated a notable decrease in the

integrated intensity ratio of I(003)/I(104) despite the formation of a complete hexagonal layered structure. Partial lithium evaporation at a high reaction time (45 min) could be one of the possible reasons. Increasing the reaction time to 60 min brought about a partial disintegration of the layered structure as can be easily discerned from the unclear splitting of (006)/(102) and (018)/(110) pairs (Figure 1B (e–i) and Figure 1C (e–ii)). The structural disintegration of Ni-rich layered oxide at high temperatures, which involves cationic disordering – i.e., the rearrangement of Ni and Li atoms leading to antisite defects such as Li_{Ni} – is known to occur when Ni-rich layered oxides are annealed at high temperatures above 850 °C. This severe cationic disorder can lead to the decomposition of the layered structure. Despite the differences in heating mechanisms between microwave and conventional annealing, extending the holding time during microwave annealing may produce similar effects to conventional annealing by allowing sufficient time for cation diffusion and rearrangement within the structure. Consequently, prolonged holding times in the MW furnace could generate a discernible fraction of cationic disorder, potentially leading to partial structural degradation. Therefore, precise control of the annealing temperature and holding time is critical to achieve a phase-pure product with minimal defects in the microwave annealing process. The XRD result shows that the MW annealing is an effective approach in producing phase pure highly crystalline Ni-rich layered oxide cathode under an optimized annealing condition. XRD refinement of all the cathodes are performed in order to determine the lattice parameters and to estimate the impurity phase fraction (For NFA-CONV, NFA-15 and NFA-60 cathode). Li_2O phase (Crystallographic information file (CIF) 1010064) is included along with the CIF file for layered oxide (CIF 1533770) while refining the pattern of cathodes having impurity phase. Table 1 provides the estimated lattice parameters along with the phase fraction. Very little variation in the lattice parameters suggest that the MW annealing quickly crystallizes the material and hence

Table 1. Crystal structure parameters of Ni-rich layered oxide cathodes with hexagonal phase acquired by Rietveld refinement of XRD patterns.				
Sample	Structural information			
	$LiNi_{0.9}Fe_{0.05}Al_{0.05}O_2$ (S.G. $R\bar{3}m$)	weight fractions (WF)		Reliability factors of refinement
	Lattice parameters (a, b, c in Å)	NFA	Li_2O (S.G. $Fm\bar{3}m$)	
NFA-CONV	$a=b=2.883$ $c=14.227$	WF = 99.4%	WF = 0.6%	$R_{wp}=9.85$ $R_p=7.18$ $\chi^2=7.33$
NFA-15	$a=b=2.879$ $c=14.215$	WF = 85.6%	WF = 14.4%	$R_{wp}=6.27$ $R_p=3.78$ $\chi^2=4.39$
FA-30	$a=b=2.881$ $c=14.228$	WF = 100%	WF = 0%	$R_{wp}=4.49$ $R_p=4.02$ $\chi^2=2.57$
NFA-45	$a=b=2.884$ $c=14.224$	WF = 100%	WF = 0%	$R_{wp}=4.19$ $R_p=2.17$ $\chi^2=4.67$
NFA-60	$a=b=2.883$ $c=14.230$	WF = 96%	WF = 4%	$R_{wp}=7.28$ $R_p=4.17$ $\chi^2=9.60$

Batteries & Supercaps

Research Article
doi.org/10.1002/batt.202400782

Chemistry
Europe
European Chemical
Societies Publishing

changes in the annealing temperatures or holding periods appear to have little effect on the structural parameters.

Additional information on the structural quality of the compounds down to the molecular level is obtained from the Raman spectra as shown in Figure S3. Despite the strong electrical conductivity of Ni-rich layered oxide cathodes, which limits Raman scattering efficiency due to their short optical skin depth, and hence, resulting in very low Raman mode intensities,[36] the Raman spectra show a broad mode, which is commonly noted for layered oxide cathode with a high concentration of nickel. [37] In general, the Raman spectra of ternary layered oxide cathode display two Raman active modes: (i) the A_{1g} mode representing the symmetric movement of oxygen ions along the c-axis and (ii) the E_g mode representing the displacement of oxygen ions along adjacent O-layers in opposite directions. NFA cathode displayed a broad peak, centered at about 540 cm^{-1}. A second Raman mode also can be discerned with very broad profile however with very low intensity. It is noteworthy that two separate Raman modes, centered at around 465 cm^{-1} and 538 cm^{-1}, with much narrow peak broadening is observed in the NFA-30 cathode, is strikingly comparable to our prior observation on the Ni-rich NCA cathode.[38] A somewhat different Raman spectrum with substantially broader feature is displayed by the NFA-60 cathode, supporting its distorted structure. In layered oxide cathodes, Raman spectra with diverse profile features are reported including variation in the intensity ratio of the A_{1g} and E_g modes from particle to particle,[36] which could be a signature of inhomogeneity, and due to the diverse possible composition formed by different transition metals (Mn, Co, Al, Fe, etc.) in Ni-rich layered oxide cathodes (Ni concentration $>60\%$). Although the Raman band position of other NFA compositions are unknown in the literature, LiNi$_{0.9}$Fe$_{0.05}$Al$_{0.05}$O$_2$ revealed Raman wavenumber at ~540 cm^{-1} which is very close to other Ni-rich NCA and NMC Raman modes.[39] The superposition of A_{1g} and E_g band of each TM—O bond makes it difficult to deconvolute the broad Raman spectra of Ni-rich layered oxide due the complex interactions between the homogeneously distributed transition metal ions.[40] Despite all such odds, the Raman spectra of MW annealed samples suggest that NFA-30 show better crystallinity and phase purity compared to the rest of the MW annealed compounds as well as the conventional annealed samples.

2.3. Morphology and Compositional Studies

The FESEM images of ternary oxide precursor are shown in Figure S4. The precursor is comprised of several microspheres with a diameter ranging from 3 to 5 μm, as shown in Figure S4. The high-resolution image reveals that each microsphere (referred as secondary particle) is made up of densely packed nanoparticles (referred as primary particles) resulting in a rough surface. The SEM images of NFA-CONV and NFA-30 cathodes are shown in Figure 2 (a), (b) and Figure 2(c), (d), respectively and the corresponding SEM images of other cathodes (NFA-15, NFA-45, and NFA-60) are shown in Figure S5, S6 and S7. The low magnification images of NFA-CONV and NFA-30 cathode is

also provided in Figure S8. Despite the high-temperature annealing, NFA-CONV cathode material retains the spherical morphology of the precursor. The average diameter of each microsphere of NFA-CONV cathode is estimated to be ~4 μm, almost similar to that of the precursor microsphere. Further examination in the magnified image (Figure 2(b)) reveals that the microspheres have a very porous texture and a hierarchical structure. The hierarchical flower-like microspheres were built from multiple curved nanosheets with an average thickness of around 10–20 nm.

The microspherical shape of the NFA-30 cathode is significantly disrupted following microwave high temperature annealing, as seen in Figure 2(c). The fast-annealing process happening at high temperature in the microwave reaction may cause anisotropic strains during the growth of primary particles of different sizes, which could be linked to the breakdown of spherical morphology. Spherical particles that do not fragment have an average diameter of ~4.5 μm. Despite the fact that the reaction periods differ by a factor of 30 between microwave and conventional process, it is noteworthy that the microspherical morphology derived from these two distinct annealing methods exhibit nearly similar particle diameters as that of ternary oxide precursor diameter (~3–5 μm). Following MW annealing, the primary particle constituting the microspheres of the NFA-30 cathodes are different in the size. The NFA-30 microspheres mostly consist of tiny nanoparticles, with an average size of approximately 300 nm (Figure 2(d)). This result suggests that while conventional and MW irradiation heating have no significant effect on the size of microspherical particles, they affect the primary particles' shape. Following MW treatment, the NFA-15 cathode also displayed spherical particles with a diameter of around 5 μm (Figure S5 (c)). The low magnification image revealed that the microspherical secondary particles are mostly shattered following the quick MW treatment (Figure S5 (a)). The notable fluctuation in the ternary oxide precursor's particle diameter (~3–5 μm) caused a significant fluctuation in the average spherical particle diameter of the NFA-CONV, NFA-15, and NFA-30 cathodes after high temperature annealing. NFA-45 and NFA-60 cathode mostly displayed big irregular particles of size ~40 μm after calcination. Spherical particles (diameter ~5 μm) observed in Figure S6 (c) and Figure S7 (c) suggest that, in the case of NFA-45 and NFA-60 cathodes, individual microspheres cluster together to produce irregularly shaped particles after the prolonged MW treatment. This finding suggests that changes in the MW reaction time have a major effect on the morphology of the secondary particles, which in turn can influence the electrochemical performance of electrodes. The energy dispersive X-ray spectral (EDS) analysis is performed on all the NFA cathode to estimate the concentration of transition metals. The X-ray photon count with the energy of characteristic X-rays acquired is presented in Figure 3 and Figure S9. All of the Ni-rich samples' elemental analyses reveal the stoichiometric compositions of the samples (see Table S1). To analyze the distribution of different elements, EDS elemental maps of Ni, Fe, Al, and O were obtained for all NFA samples, as shown in Figure 3 and Fig S10. A single spherical particle is used to carry out the elements
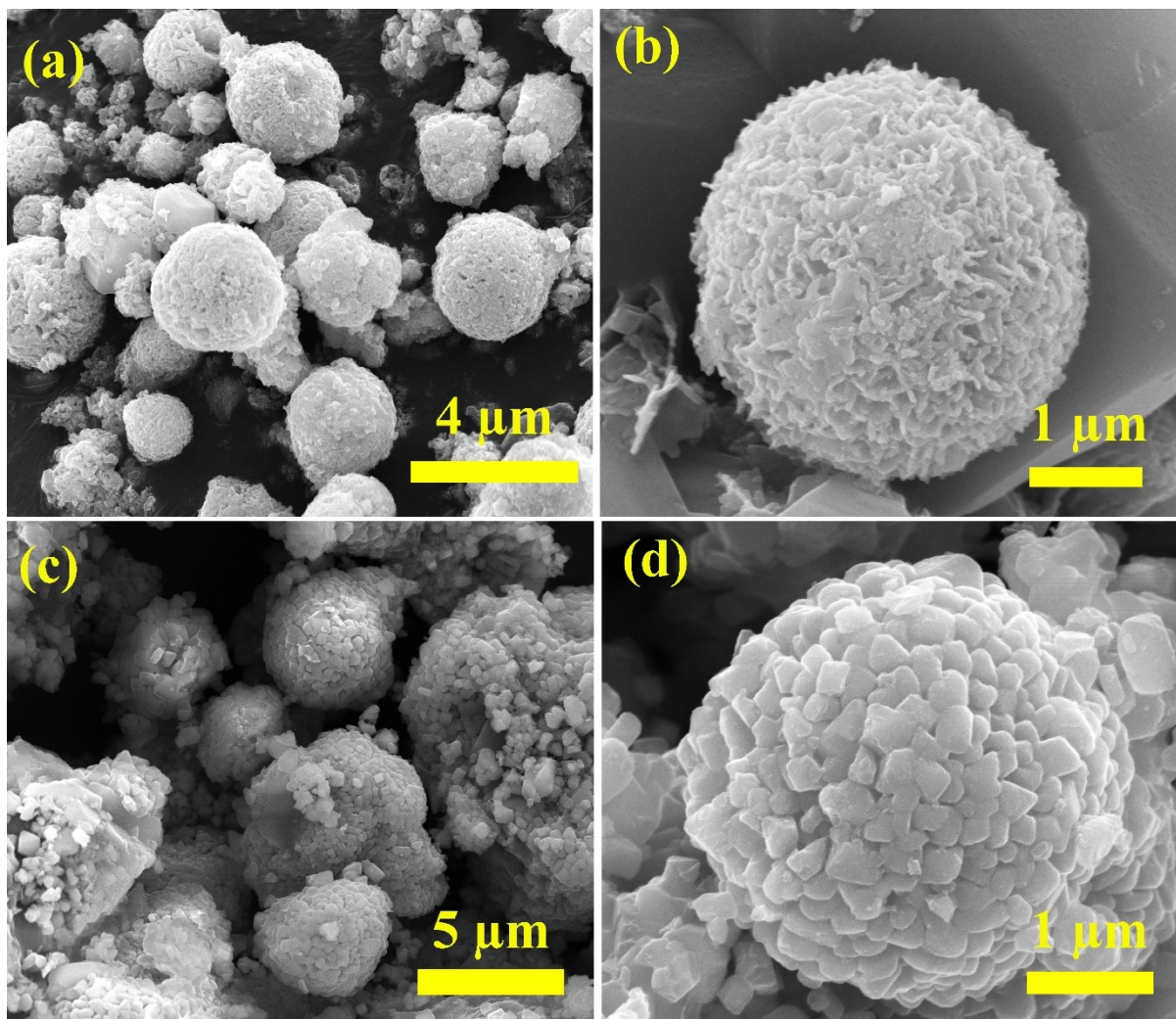
Figure 2. Field emission scanning electron microscopy images of (a) NFA-CONV, and (c) NFA-30 Ni-rich layered oxide cathode materials. The magnified images of (a) and (c) are shown in (b) and (d), respectively.

mapping for the NFA-CONV, NFA-15, and NFA-30 cathode. On the other hand, agglomerated particle is used to perform the elemental analysis in case of NFA-45 and NFA-60 cathode. However, to further confirm the homogeneity of the elements present in the NFA-30 cathode which display both spherical and non-spherical (fragmented) particles, the elemental mapping is performed in the fragmental particles (Figure S11). The low magnification EDS mapping also revealed the homogeneity of the elements in the cathode, regardless of whether the particles are spherical or non-spherical. The presence of homogeneous characteristic X-ray intensity indicates the uniform distribution of various transition metals and oxygen in all the materials.

2.4. XPS Studies

To determine the oxidation states of each NFA cathode and to comprehend the surface chemical structure, XPS studies were performed. Figure 4 displays the XPS spectra of all the samples.

A broad peak can be seen at about 55 eV in the Li 1s spectra of all the NFA cathodes (Figure 4(a)). While NFA-15, NFA-30, and NFA-45 cathodes have nearly identical peak positions (~55.1 eV) in the Li 1s binding energy, NFA-CONV (~55.4 eV) and NFA-60 (~55.2 eV) cathodes show a slightly higher binding energy in Li 1s spectra. Li_2O, which exhibits a photoemission peak at around 55.6 eV, may be a contributing factor.[41] Notably, the binding energy of all the NFA Li 1s core spectra is found to be 0.6–0.9 eV higher than the reported Li 1s binding energy value reported for Ni-rich layered oxide cathodes (~54.5 eV).[42,43] A thin coating of Li_2CO_3 and LiOH is produced (as corroborated by the O 1s and C 1s spectra) on the surface of the Ni-rich cathode as a result of the substantial side reaction of excess lithium with atmospheric CO_2 and water molecules. The existence of surface-absorbed species, which show binding energy values of ~55.3 eV (Li_2CO_3) and ~54.9 eV (LiOH), causes the Li 1s core binding energy of all the NFA cathodes appear at higher BE values.[44] The presence of surface absorbed species is highly noticeable in the O 1s spectra as shown in Figure 4(b). Every sample's O 1s core spectra display a strong peak centered at
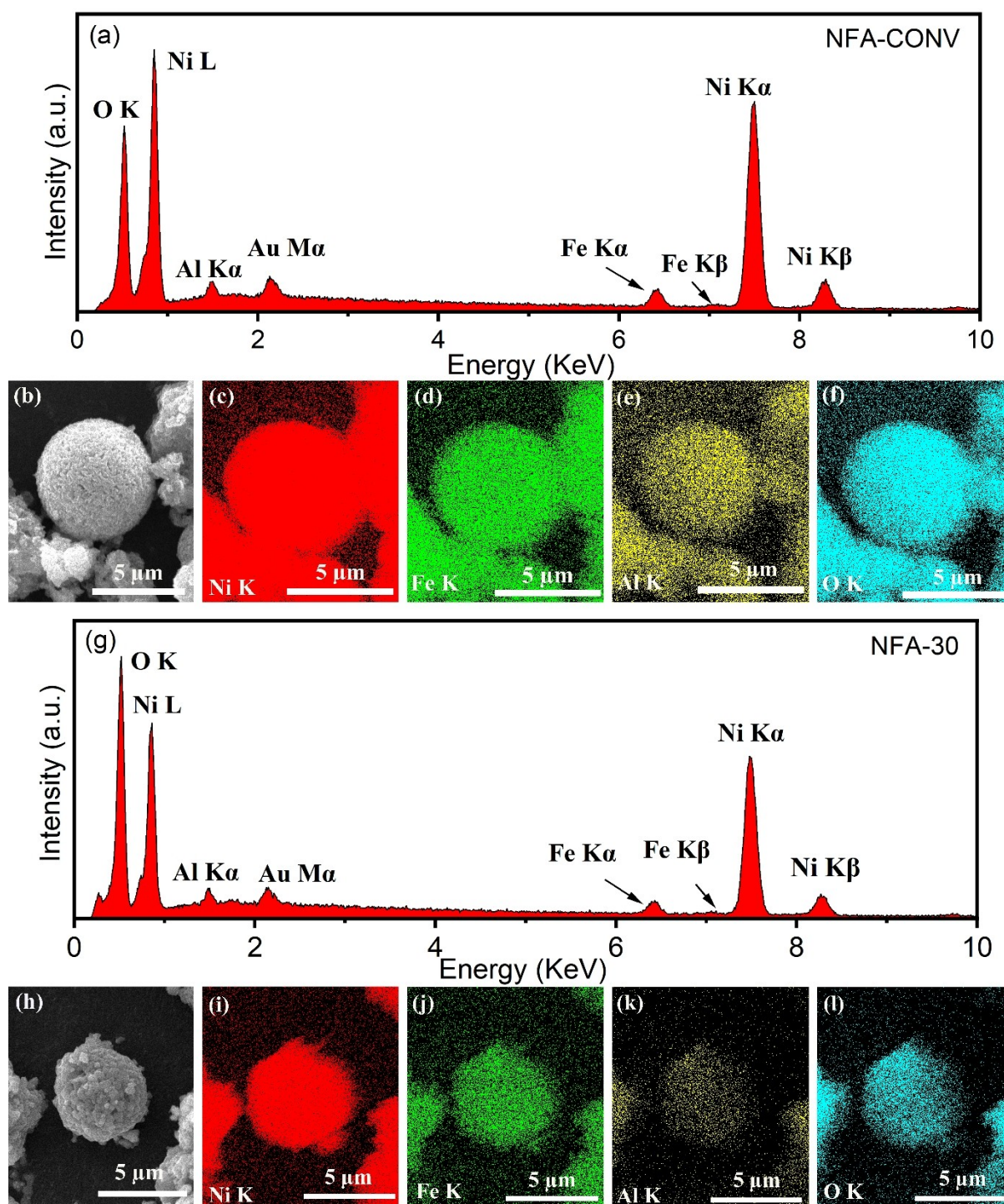
Figure 3. Energy dispersive X-ray spectra of (a) NFA-15, and (g) NFA-30 cathode. Energy dispersive X-ray elemental mapping of (b)–(f) NFA-CONV, and (h)–(l) NFA-30 cathode. Au X-ray lines (Mα peak at around 2.2 keV) observed in all samples result from gold sputter coating performed to inhibit the charging effect during imaging. Single spherical particle have been taken for elemental mapping for the two cathodes.

about 531.3 eV. Furthermore, all cathodes exhibit a core spectral peak at ~528.7 eV, as seen in Figure 4b. While O^{2-} anions in the crystalline lattice are represented by the core spectra centered at ~528.7 eV, O 1s core spectra with binding energy ~531.3 eV are linked to surface adsorbed chemical species such as O—C=O.[45] The existence of surface-absorbed

H_2O can be connected to a tiny peak in the O 1s spectra that is seen at around 534 eV.[46] Notably, in the case of the MW treated cathode, the strength of the surface absorbed carbonate peak is more than that of the lattice oxygen peak, indicating the presence of additional layers of carbonate and hydroxide species of a few angstroms on the surface. Differ-
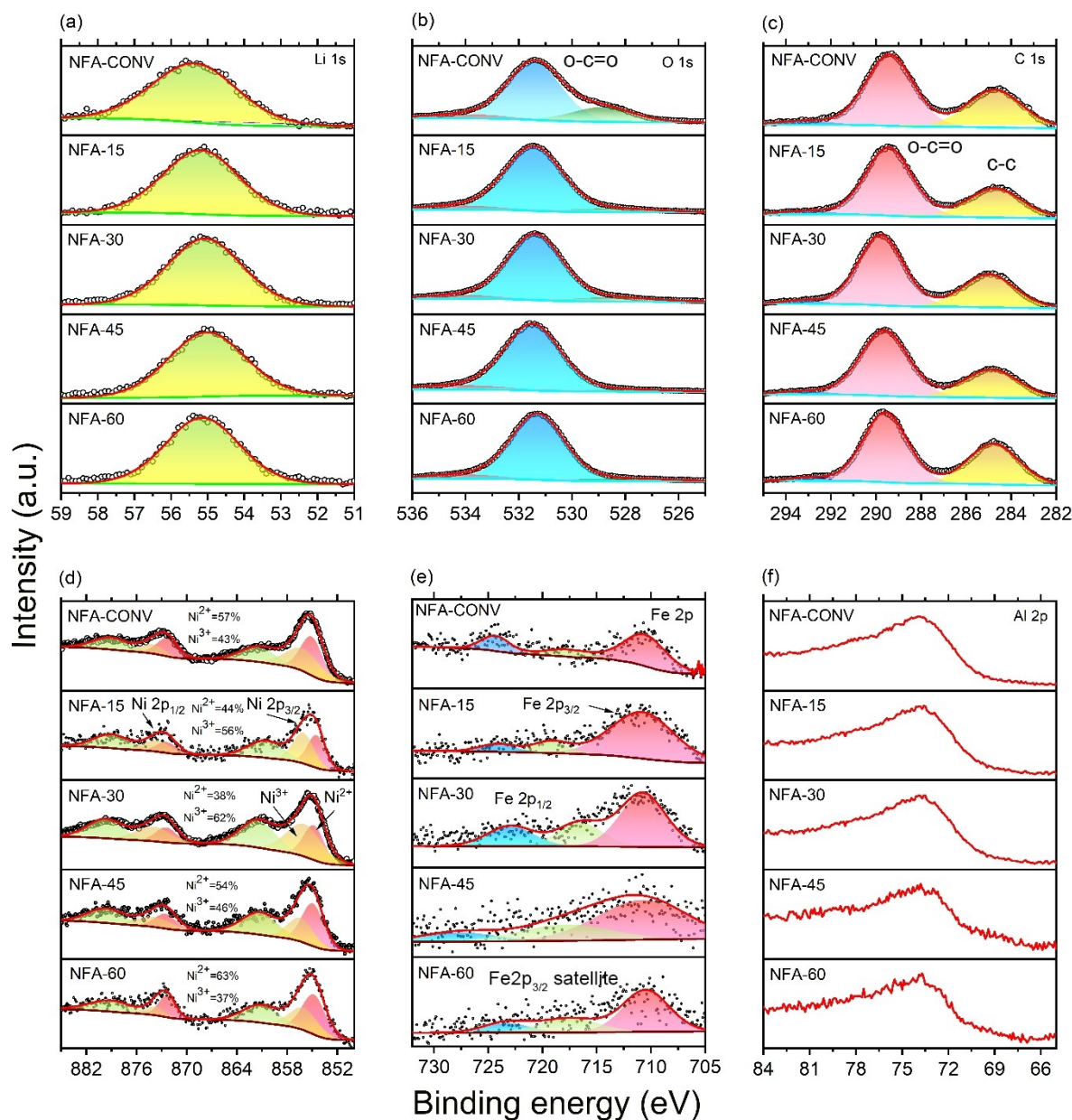
Figure 4. X-ray photoelectron spectra of Ni-rich layered oxide showing (a) Li 1s, (b) O 1s, (c) C 1s, (d) Ni 2p, (e) Fe 2p, and (f) Al 2p spectra for all the Co-free, Ni-rich layered oxide samples. In (b) the spectrum is deconvoluted for lattice O (green shaded) and O–C=O (blue shaded). In (c) the spectrum is deconvoluted for characteristic carbon (yellow shaded) and O–C=O (pink shaded). In (d) the spectrum is deconvoluted for Ni^{2+} (pink shaded), Ni^{3+} (dark yellow shaded), and satellite (light green shaded). In (e) the spectrum is deconvoluted for Fe $2p_{3/2}$ (pink shaded), Fe $2p_{1/2}$ (blue shaded), and satellite (light green shaded). The black symbols correspond to data acquired in XPS and the red lines are fitted curves.

ences in primary particle morphology could be one of the possible reasons. Figure 4(c) confirms the presence of O–C=O by displaying a C 1s peak at ~289.7 eV for all samples. Based on the XPS study and analyzing the integrated area of the O–C=O peak and the carbon C–C peak from the C 1s core spectra, no clear correlation between the microwave reaction time and the quantity of Li_2CO_3 or LiOH is observed. This is also evident from the XRD, Raman and FTIR characterization of these materials (Figure S12).

Figure 4(d) displays Ni 2p XPS spectra with two distinct peaks at ~855 eV and ~873 eV, representing the binding energy of Ni $2p_{3/2}$ and Ni $2p_{1/2}$ core spectra, respectively.[46] Multiple splitting of energy levels of transition metals results in the satellite peak of Ni 2p, which is represented by the light green shaded peaks.[47] Due to the presence of two different oxidation state (Ni^{2+} and Ni^{3+}), the photoelectron spectra of Ni 2p ($Ni2p_{3/2}$ and $Ni2p_{1/2}$) can be deconvoluted into two peaks, with the former ranging from 854.5 to 854.9 eV (Ni^{2+}) and 855.9 to 856.2 eV (Ni^{3+}), and the latter ranging from 872.2 to 872.5 eV (Ni^{2+}) and 873.6 to 874.1 eV (Ni^{3+}). The proportion of Ni^{2+} and Ni^{3+} on the surface of the cathode particle is determined from the integrated peak intensities of Ni^{2+} and Ni^{3+}, and the

Batteries & Supercaps

Research Article
doi.org/10.1002/batt.202400782

Chemistry
Europe
European Chemical
Societies Publishing

corresponding values are shown in Figure 4(d). The increased Ni^{2+} oxidation state on the surface of the NFA-CONV, NFA-45 cathode may be the cause of the increased cationic disorder in its layered lattice. Less Ni^{2+} is detected on the surface of the NFA-15 and NFA-30 cathodes, indicating greater Ni^{2+} oxidation into Ni^{3+} during synthesis, which successfully suppressed the cationic disorder in the layered structure for both cathodes. This observation is consistent with the XRD results, which also indicate a similar cationic disordered structure prevailing in the NFA-CONV and NFA-45 cathodes, as indicated by the intensity ratio of I(003)/I(104). Fe $2p$ spectra (Figure 4(e)) mostly display characteristics of the Fe^{3+} oxidation state as discerned from the binding energy of Fe $2p_{3/2}$ (at 710.8 eV) for all the samples. For Fe^{3+}, satellite peaks typically occur at 8 eV above $2p_{3/2}$, while for Fe^{2+}, they appear at 6 eV above $2p_{3/2}$. The 3 + oxidation state of Fe is further confirmed by the appearance of a satellite peak ~7.4 eV above Fe $2p_{3/2}$ in all of the NFA cathodes. Al $2p$ spectra of all the cathode showed a broad peak centered at ~73.5 eV (Figure 4(f)). The Al $2p_{3/2}$ and $2p_{1/2}$ peaks' tiny spacing (0.44 eV) eventually results in a broad signal that appears as a single peak. The presence of broad peak at ~73.5 eV illustrates the presence of Al^{3+} for all the samples.

2.5. Electrochemical Studies

Galvanostatic charge-discharge tests are performed on all the cathodes at 0.1 C-rate for five cycles. These first five galvanostatic charge-discharge curves are shown in Figure S13. It should be noted that NFA-CONV, NFA-15, and NFA-30 cathodes show almost similar charging and discharging profiles as reported in the literature for layered oxide cathodes, such as NMC ($LiNi_xCo_yMn_zO_2$, $x > 0.6$).[48] The charging profile of all the cathodes showed a slopping profile up to 4.5 V which substantiates the oxidation of Ni^{2+} to Ni^{3+} and subsequently Ni^{3+} to Ni^{4+}.[49] During the very first de-lithiation (charging), NFA-CONV, NFA-15, and NFA-30 cathode delivered a high charging capacity of 240.0, 230.2, and 242.2 mAh g^{-1} (Figure S13 (a)–(c)) which substantiates the oxidation of most of the Ni^{3+} to Ni^{4+} during charging. During the first discharge, NFA-CONV cathode shows a profile with a sloping potential up to the lower cutoff voltage (~2.8 V). NFA-CONV cathode exhibits a lithiation (discharging) capacity of 177.1 mAh g^{-1} at the very first cycle with a coulombic efficiency (CE) of 73.7%. It is noteworthy that the NFA-CONV cathode's discharging capacity increases from 177.2 mAh g^{-1} to 194 mAh g^{-1} (Figure S13 (a)) in the following cycle, which may be the result of the electrode's initial activation. NFA-15 cathode delivered a discharge capacity of 176 mAh g^{-1} (Figure S13 (b)) at the very first cycle and a CE of 77.4%. It should be noted that the discharge capacity rapidly fades in the first five cycles at 0.1 C-rate for NFA-15 cathode. Possible reasons include surface degradation, presence of impurities, and oxygen evolution.[50] During the initial lithiation, NFA-30 outperformed all other cathodes in terms of first lithiation capacity (184.4 mAh g^{-1}) and high CE (82%) (Figure S13 (c)). It should be noted that the initial discharge profile for NFA-15 and NFA-30 cathode is quite similar to that of NFA-

CONV cathode. After five cycles, the activation procedure caused the lithiation capacity to grow to 195.5 mAh g^{-1} for NFA-30 cathode. The MW-delivered Co-free NFA-30 cathode's high discharge capacity is nearly identical to that of other Co-containing commercial Ni-rich layered oxides, like NCA and NMC. After the first discharge, the subsequent cycles of charging-discharging show high reversibility in NFA-CONV, NFA-15, and NFA-30 cathode with nearly 100% CE. The first charging and discharging capacities of NFA-45 cathode (Figure S13 (d)) are 200.9 mAh g^{-1} and 148.8 mAh g^{-1} (CE of 74.1%). During the charging and discharging processes, the cathode displays a somewhat distinct voltage profile. The electrode polarization, which may be the result of metal ion migration in the layered structure, can be connected with the greater average charging voltage and the lower average discharging voltage for the NFA-45 cathode. Li^+ deficiency at longer reaction times can also be connected with a decrease in charge-discharge capacity. The huge irregularly shaped NFA-45 cathode particle may have an effect on the electrochemical performance because of its large diffusion path length which potentially impede the migration of charge carriers inside the particles. The first cycle charging capacity for NFA-60 is ~152.3 mAh g^{-1}. The cathode delivered a low discharging capacity of ~102.3 mAh g^{-1} (Figure S13 (e)) in the very first cycle. The poor electrochemical performance of the NFA-60 cathode can be correlated with its distorted layered structure.

To understand the redox reaction mechanism of NFA-CONV and MW derived cathodes, a cyclic voltammetry test is performed at 0.05 mV/sec. Figure 5(a) and (b) show the cyclic voltammetry curves of NFA-CONV and NFA-30 cathodes, and the equivalent CV curves of additional MW-derived cathodes (NFA-15, NFA-45, and NFA-60) are shown in Figure S14 (a)–(c). The NFA-CONV and NFA-30 cathodes show a couple of anodic (charging) redox peaks at around ~3.8, ~4.0, and ~4.2 V which can be correlated with Ni redox features along with crystallographic phase transition in Ni-rich layered oxide cathodes. The peaks at ~3.8, ~4.0, and 4.2 V correspond to the phase transition from hexagonal to monoclinic (H1 to M), monoclinic to hexagonal (M to H2), and hexagonal to hexagonal (H2 to H3) phases, respectively.[51] A similar kind of behavior is also reported for Co-containing Ni-rich layered oxide.[38] The Li-ion insertion into the de-lithiated layered oxide generates a cathodic (discharging) peak at ~4.0 and 3.66 V which can be connected with the reduction of Ni^{4+} to Ni^{3+}. Remarkably, the peak current measured in the anodic and cathodic sweeps of the NFA-30 cathode is greater than that of the NFA-CONV cathode, suggesting that the MW-derived cathode has more electroactive species available for the redox process. The observation from the CV profile underscores the electrochemical and chemical insertion/extraction of Li ions in the Co-free NFA framework. The redox peaks' presence at the intended voltage provides more evidence of the material's structure. Both NFA-CONV and NFA-30 cathode result in almost similar electrochemical behavior for layered oxide cathodes, as evidenced by the almost identical positions of the redox peaks in the voltammetry profile. Even though the relative peak intensities (the peak at 3.8 V) and the obvious peak splitting
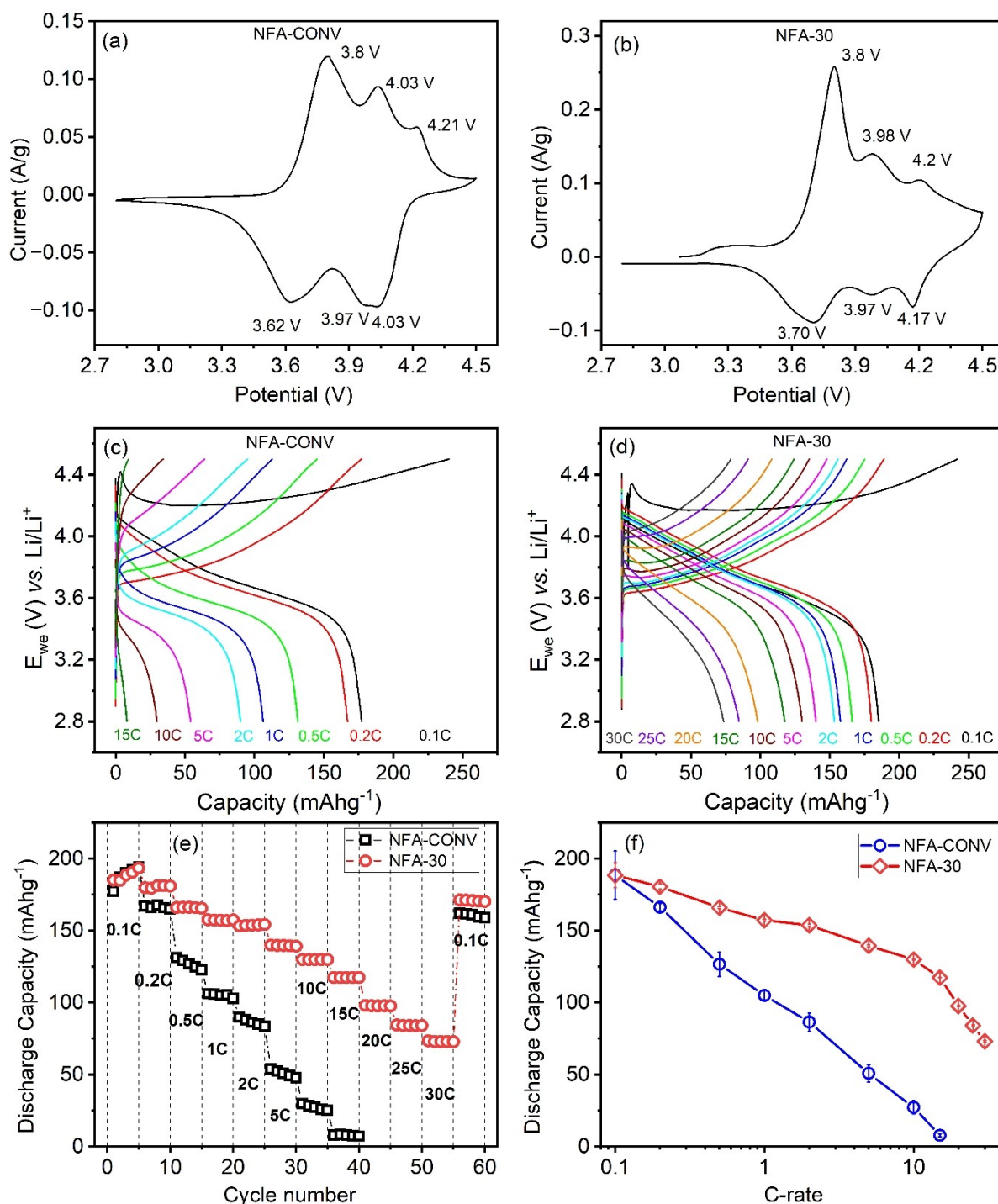
Figure 5. (a, b) Cyclic voltammetry profiles at 0.05 mV/s scan rate and (c, d) Galvanostatic charge-discharge profiles at different C-rates of (a, c) NFA-CONV and (b, d) NFA-30 cathode. (e) Plots of capacity *vs.* cycle number at different C-rates of both the cathode. (f) The average discharge capacity and the standard deviation at each scan rate as obtained from (e). The range of capacity variation at each C-rate is indicated by the vertical bar in (f).

during the cathodic sweep of the CV profiles of the NFA-CONV and NFA-30 cathodes appear to be little different, these differences may have a substantial impact on the charge storage properties of both cathodes. Despite having poor electrochemical performance, it is interesting to note that the NFA-CONV cathode demonstrated a more reversible CV profile

than the NFA-30 cathode. It should be mentioned that while the peak current of the oxidation peaks of NFA-45 and NFA-60 cathodes, at approximately 3.88 V and 3.84 V, is comparable to that of the NFA-30 cathode, the strength of other peaks is much lower in both the anodic and cathodic sweep. For both the NFA-45 and NFA-60 cathodes, the peak intensities of the

cathodic sweep are significantly lower than those of the anodic sweep, confirming the electrode's irreversible nature. This provides even more evidence for the NFA-45 and NFA-60 cathode's subpar electrochemical performance.

Owing to the NFA-30 cathode's superior charge storage property, additional electrochemical characterizations of this specific optimized cathode (NFA-30) are being conducted, and the outcomes have been compared with those of the NFA-CONV cathode. To examine the charge storage capabilities as a function of current rates, both NFA-CONV and NFA-30 cathodes that had previously been cycled at 0.1 C-rate were further cycled at various current rates, and the representative voltage profiles are displayed in Figure 5(c) and (d). The discharge capacity of the NFA-CONV cathode showed a significant reduction as a function of increasing C-rates and the cathode could work up to 15 C-rate. As the C-rate increased, the NFA-CONV cathode displayed a sharp decline in average discharge voltage, which suggests significant polarization losses. Even at 0.5 C-rate, a deviation from the ideal voltage profile (as 0.1 C-rate) is observed for the NFA-CONV cathode. NFA-30 cathode showed excellent rate capability at higher C-rates. Even at 10 C-rate, the cathode displayed the ideal voltage profile of a layered oxide cathode, demonstrating the NFA-30 cathode's better kinetics at higher C-rates. The cathode synthesized by MW annealing (NFA-30) is cyclable for up to 30 C-rate indicating the excellent rate-capability of NFA-30 cathode.

To illustrate the striking disparity in the electrochemical performance of the two cathodes at higher C-rates, a separate plot showing the capacity vs. cycle number performed at different C-rates is provided in Figure 5(e). Every C-rate undergoes five cycles of charge-discharge measurements. The average discharge capacity and the standard deviation at each scan rate are shown in Figure 5(f). The two plots make the NFA-30 cathode's strong rate capabilities very evident. Despite showing a capacity degradation with a rising C-rate, the NFA-30 cathode delivered a higher discharge capacity at each C-rate than that of the NFA-CONV cathode. The cathode showed almost 5 times higher discharge capacity than the NFA-CONV cathode at 10 C-rate. It is fascinating to see that when the C-rate rises, the two cathodes' discharge capacities diverge more at each C-rate. Remarkably, over the course of the five charge-discharge cycles in each C-rate, the NFA-CONV cathode demonstrated a capacity loss as shown in Figure 5(e). The standard deviation figure (blue line) makes these losses quite evident. However, there was no discernible capacity degradation for the NFA-30 cathode during the 5 charge-discharge cycle at each C-rate, which demonstrated a steady discharge capacity at every C-rate. Except for the very first charge-discharge cycle at each C-rate, the other cycles show nearly 100% CE for both the cathode, as shown in Figure S15 (a) and (b). At the highest tested C-rates, the average discharge capacity obtained from NFA-CONV is ~7.8 mAh g^{-1} (at 15 C-rate), and from NFA-30 is ~78.1 mAh g^{-1} (30 C-rate). It is to be noted that NFA-30, when cycled at 30 C, retained over one-third of the capacity achieved at 0.1 C cycling, indicating the excellent rate capability characteristics of the MW-treated cathode (NFA-30). The poor rate performance and the capacity

degradation of NFA-CONV cathode can be attributed to structural degradation due to metal ion migration, oxygen evolution, or both. It is noteworthy that the MW-derived NFA cathode has produced better rate performance than the NFA-CONV cathode, even though a thick coating of Li residue has formed on its surface (as evidenced from XPS analysis). Following the high current rate investigations, both cathodes were cycled at 0.1 C-rate to determine the amount of recovered capacity and to investigate the reversibility. NFA-CONV and NFA-30 cathode delivered a discharge capacity of ~161.9 mAh g^{-1} (90.1% capacity retention) and ~171.3 mAh g^{-1} (91.8% capacity retention), respectively, almost the same as that of the initial discharge capacity before high current cycling, indicating excellent reversibility of both the cathodes.

To shed light on how MW annealing affects the cyclic performance of Ni-rich layered oxide (NFA) cathodes, new cells of NFA-CONV and NFA-30 cathodes are created and evaluated for 100 cycles at a rate of 1 C in the voltage range of 2.8–4.5 V vs. Li/Li$^+$. Figure 6(a) shows the cyclic performance of NFA-CONV and NFA-30 cathodes. The undulations in discharge capacity as a function of cycle number are caused by temperature fluctuations in the lab. NFA-CONV and NFA-30 cathodes showed discharge capacities of 100.3 mAh g^{-1} and 141 mAh g^{-1} during the first cycle, respectively. Upon extensive cycling, the discharge capacity of NFA-CONV cathode decreases drastically from 100.3 mAh g^{-1} to 37.8 mAh g^{-1} with a capacity retention of 37.6% only. The discharge capacity of NFA-30 drops from 141 mAh g^{-1} to 110.2 mAh g^{-1} after 100 cycles and exhibits capacity retention of 78.1%. Figure S16 (a) and (b) demonstrate that the cathode's coulombic efficiency is about 100% for every cycle, with the exception of the first one or two cycle. The structural integrity (See the post-electrochemical study section in the Supplementary Information) of the NFA-30 cathode material helps to maintain its cyclic stability throughout cycling. The voltage stability of the two cathodes were evaluated at 1 C-rate on the same cell that had undergone a 100 charge-discharge cycles. Figure 6(b) show the average discharge voltage as a function of the number of charge-discharge cycles for NFA-CONV and NFA-30 cathode, respectively. Although the intrinsic phase change, together with the rise in impedance during the charge-discharge cycle, leads in a voltage drop for both the cathode throughout the charge-discharge cycle, NFA-CONV cathode suffered significant voltage drop as compared to NFA-30 cathode. After 100 cycles, the average discharge voltage decreases from 3.66 V to 3.44 V at a rate of 2.2 mV/cycle, implying significant polarization loss, structural degradation, and phase change for the NFA-CONV cathode. In contrast, NFA-30 cathode showed very minimal voltage reduction (0.4 mV/cycle), indicating strong structural integrity as well as modest increase in internal impedance. The typical charge-discharge profiles (1st, 25th, 50th, 75th, and 100th) displayed in Figure 6(c) for NFA-CONV and Figure 6(e) for NFA-30 cathode make this stark difference in voltage stability very clear. As the cycling proceeds, the potential differential on mid-capacity grew from 320 mV to 660 mV (increased by 340 mV) after 100 cycles for the NFA-CONV cathode, and from 165 mV to 215 mV (increased by 50 mV) for the NFA-30 cathode. The extreme tilt in the
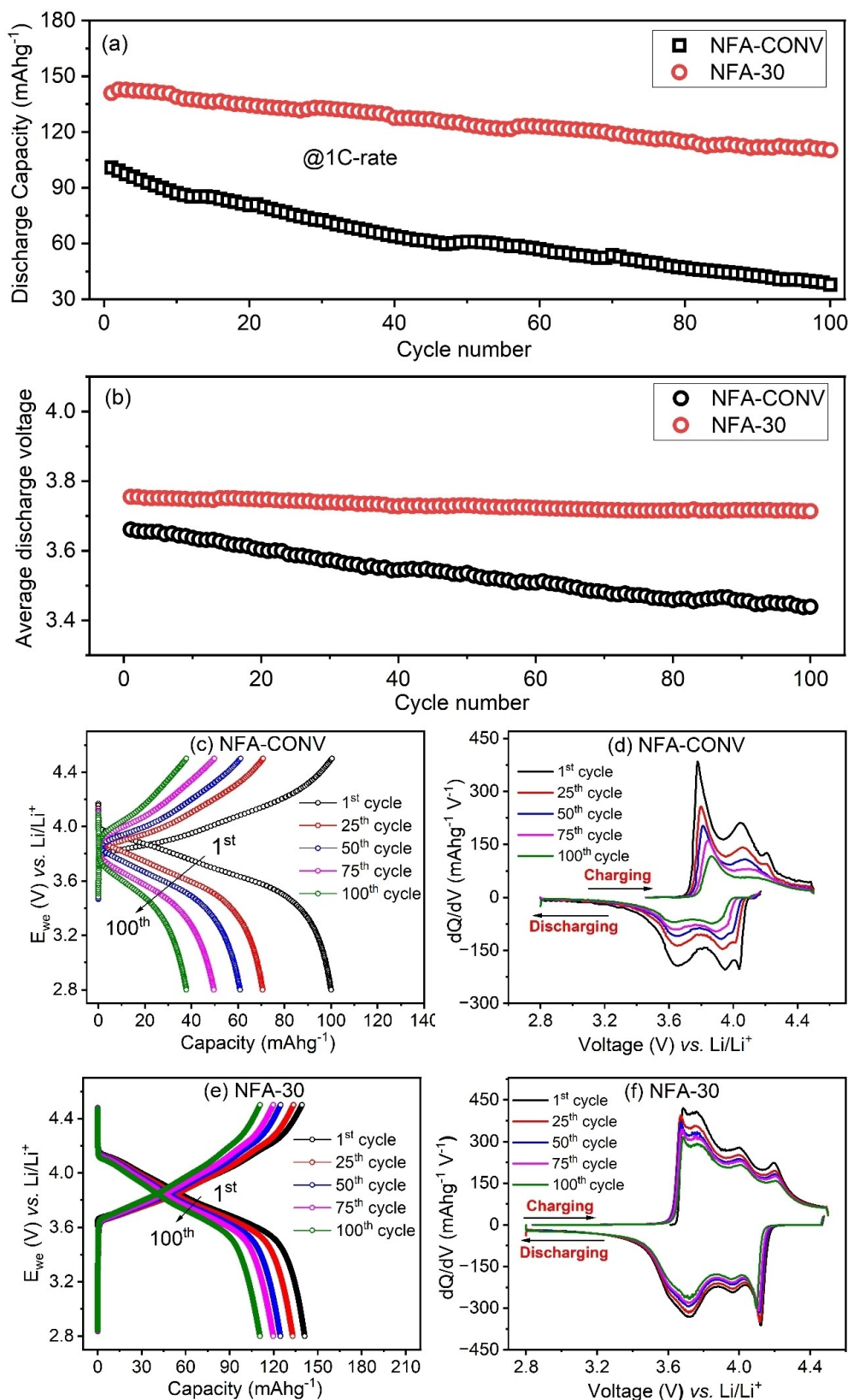
Figure 6. (a) Capacity versus cycle number of at 1 C-rate for 100 cycles. (b) Average voltage vs. cycle number plot of NFA-CONV and NFA-30 cathodes at 1 C-rate for 100 cycles. Charge discharge curve at 1st, 25th, 50th, 75th and 100th cycle for (c) NFA-CONV, and (e) NFA-30 cathode. Corresponding dQ/dV plots at 1st, 25th, 50th, 75th and 100th cycle for (d) NFA-CONV, and (f) NFA-30 cathode. The fluctuations in the discharge capacity as a function of cycle number is due to the fluctuation in the air-conditioned lab temperature.

Batteries & Supercaps

Research Article
doi.org/10.1002/batt.202400782

Chemistry
Europe

European Chemical
Societies Publishing

discharge profile during cycling suggests significant impedance growth for the NFA-CONV cathode. The relatively little variation in the average discharge voltage clearly demonstrates the structural stabilization of MW-annealed (NFA-30) cathode, which leads to unaltered ordered layered structure, as explained in the post-electrochemical study section in the supplementary information (Figure S18).

The differential capacity *vs.* voltage profile (Figure 6(d), (f)) is derived from the charge-discharge curves corresponding to the 1st, 25th, 50th, 75th, and 100th cycles in order to gather further information on the structural alterations of both cathodes. Each plot shows couple of oxidation and reduction peaks which substantiates phase transitions. The phase transitions from hexagonal to monoclinic (H1 to M), monoclinic to hexagonal (M to H2), and hexagonal to hexagonal (H2 to H3) phases are represented by the peaks at around 3.7 V, 4.0 V, and 4.2 V, respectively.[52] The gradual decline in intensity of oxidation and the reduction peaks (Figure 6(d)) during cycling further corroborate the poor structural integrity of the NFA-CONV cathode. It is noteworthy that the strength of H2–H3 phase transition diminishes almost and disappear after 50th cycle, indicating low reversibility of the H2–H3 phase transition, which significantly contributes to progressive phase change for the NFA-CONV cathode. The poor reversibility of the H2–H3 phase transition is one of the primary causes of the NFA-CONV cathode's poor cycle stability. The strength of all the oxidation and reduction peaks, as well as the H2–H3 phase transition peak changes little during 100 cycles for NFA-30 cathode suggesting better structural stability and excellent reversibility, which played a major role in delivering better capacity retention for NFA-30 cathode after 100 charge-discharge cycle.

The effect of MW annealing on Li-ion diffusion is investigated using cyclic voltammetry at scan rates ranging from 0.1 to 1 mV/s. Figure 7(a) and (c) shows the cyclic voltammetry curves of NFA-CONV and NFA-30 cathode at different scan rates. Because of electrode polarization, at all scan rates, the anodic and cathodic peak separation rises with scan rate. It is noteworthy that the anodic redox peak intensities at around 4.0 and 4.2 V are not readily discernible for the NFA-CONV cathode at scan rates between 0.1 and 1 mV/s, however the peak intensities are clearly evident in case of NFA-30 cathode in all scan rates. The strength of the cathodic peaks (at ~4.0 and 3.66 V) in the NFA-CONV cathode diminishes with increasing scan rate, indicating poor Li diffusion kinetics. The calculation of the diffusion coefficient is estimated using the Randles-Ševčík equation (1),

$$\frac{i}{m} = 0.446F\left(\frac{F}{RT}\right)^{\frac{1}{2}} C_{Li} \ v^{1/2} \ A_e \ D^{1/2} \tag{1}$$

where $\frac{i}{m}$ is the normalized peak current (A/g), F is the Faraday constant (96485.33 C mol^{-1}), R is the Universal gas constant (8.314 J mol^{-1} K^{-1}), C_{Li} is the concentration of Li ions (mol cm^{-3}), v is the scan rate (V s^{-1}), 'A_e' is the active surface area of the electrode materials (cm^2) and D is the diffusion coefficient (cm^2 s^{-1}). The Randles-Ševčík fit for the NFA-CONV and NFA-30 cathode is shown in Figure 7(b) and Figure 7(d), respectively.

The fit shows that the intensity of the peak current varies linearly as a function of the square root of the scan rate, implying that the reaction is diffusion-limited.[53] The calculated anodic and cathodic diffusion coefficients of both NFA-CONV and NFA-30 cathodes are given in Figure 7(b) and Figure 7(d). The diffusion coefficient of the NFA-30 is higher than that NFA-CONV cathode, which is in good agreement with the rate capability results of NFA-30 cathode. Diffusion coefficient of NFA-CONV and NFA-30 cathode is also estimated using GITT technique (Figure 7(e) and (f)) to obtain the information of Li-ion diffusion kinetics as a function of potential. The corresponding variation in the diffusion coefficient as a function of voltage is shown in Figure 7(g) and (h). The diffusion coefficient first increased significantly up to 3.85 V and remained almost constant up to 4.1 V for NFA-30 cathode. During successive de-lithiation (> 4.1 V), the diffusion coefficient decreases with charging voltage, which might be related to the constriction of the Li slab along the *c* axis (owing to H2–H3 phase transition) at high charge states, impeding Li ion transport. To demonstrate the changes in the lattice parameters as a function of charging, the XRD pattern of the cathode foil was recorded at different charging voltages ranging from 3.8 V to 4.5 V in 0.2 V increments (Figure S17). The changes in the diffraction peak position of (003) primarily correspond to alterations in lattice parameter along the c-axis direction. Figure S17 shows that the (003) peak initially shifts to lower 2θ values until 4.2 V, after which it rapidly shifts to higher 2θ, even exceeding the position observed at 3.8 V. According to Bragg's law, this indicates that the c-axis lattice parameter first expands up to 4.2 V before undergoing significant contraction. The shift in the (003) peak location clearly reflects variations in the c-axis lattice parameter during charging, further supporting the observed reduction in the diffusion coefficient beyond 4.1 V. Very little variation in the diffusion coefficient is observed in case of NFA-CONV cathode during charging. It is clear from Figure 7(g) that the diffusion coefficient of NFA-30 is higher in magnitude compared to NFA-CONV at all potentials except at the beginning (< 3.7 V). From the GITT result we infer that the diffusion coefficients are of the order of 10^{-11} to 10^{-10} cm^2 s^{-1} during charging and discharging for Co-free LiNi$_{0.9}$Fe$_{0.05}$Al$_{0.05}$O$_2$ cathode which is very close to that obtained from the CV analysis.

An AC impedance measurement is performed on the cells both after 1st cycle and after 100th cycle to comprehend the impact of microwave radiation on the conductivity of electrodes (Figure 8). The measurements are performed on NFA-CONV and NFA-30 cathode in their fully charged condition. Similar characteristics were displayed by both cathodes in the impedance plot both before and after the cell underwent cycling. Z-fit software is used to fit the received EIS data to an analogous circuit (shown in the inset of Figure 8) to obtain the impedance parameters (built in the Biologic electrochemical workstation). In addition to the acquired EIS data, Figure 8 also shows the simulated Fit (Red color) that was derived from the equivalent circuit. Two semicircles and a low-frequency slope make up each Nyquist plot for both the cathodes. The resistance encountered by the Li$^+$ ion passing through the electrolyte (R$_s$ in the equivalent circuit) is represented by the

Batteries & Supercaps

Research Article
doi.org/10.1002/batt.202400782

Chemistry Europe
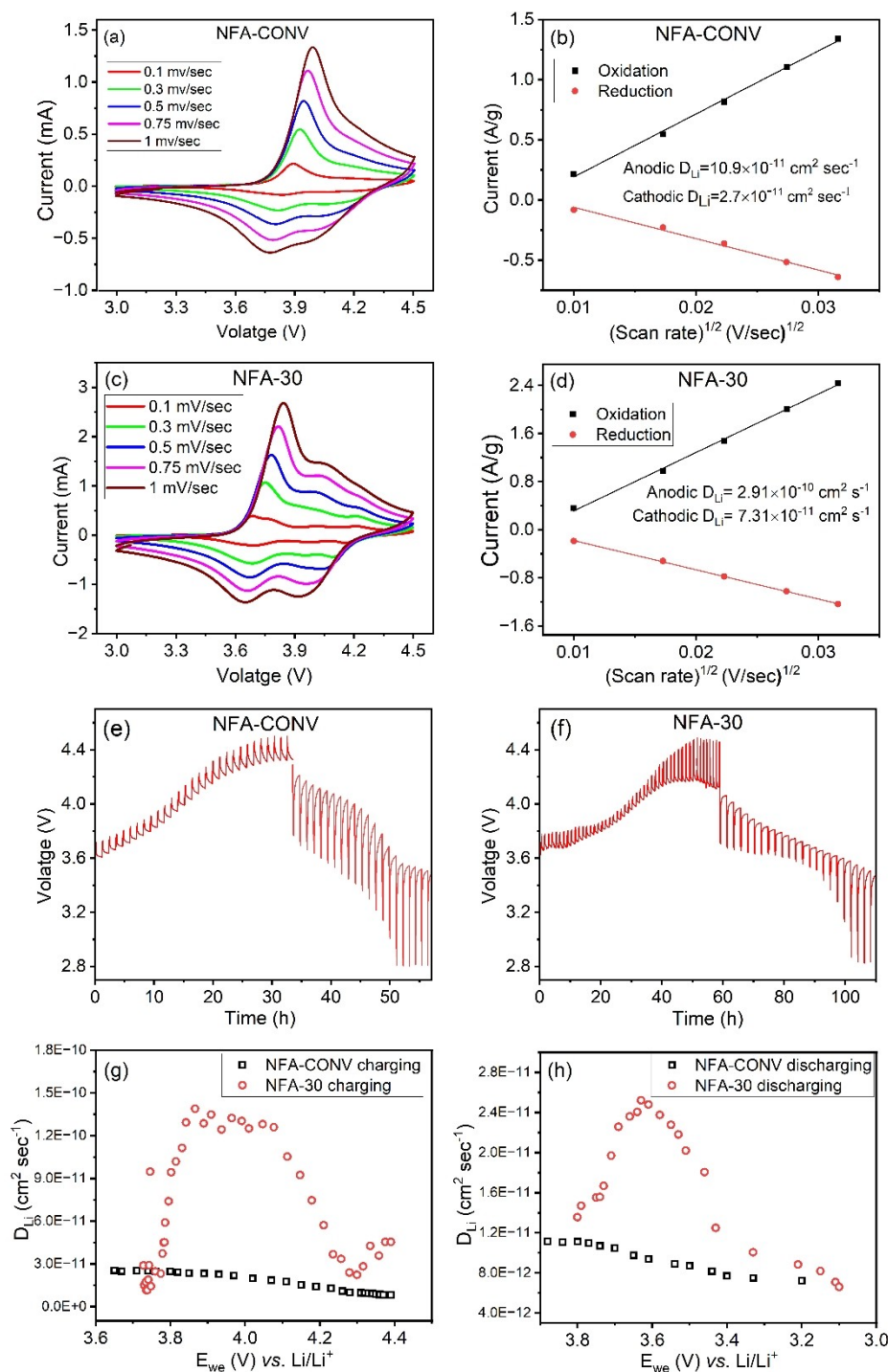European Chemical
Societies Publishing

Figure 7. (a) Cyclic Voltammetry profile at different scan rates measured at room temperature for NFA-CONV cathode. (b) The plots of anodic and cathodic current vs. square root of scan rate are shown for the NFA-CONV cathode. (c) Cyclic Voltammetry profile at different scan rates measured at room temperature for NFA-30 cathode. (d) The plots of anodic and cathodic current vs. square root of scan rate are shown for the NFA-30 cathode. (e) and (f) Galvanostatic intermittent titration technique (GITT) curve of NFA-CONV and NFA-30 cathode at 0.1 C-rate in the voltage of 2.8–4.5 V. (g) and (h) The corresponding chemical diffusion coefficients as a function of potential during charging and discharging, respectively.

intercept of the first semicircle with the real axis in the high-frequency region.[54] The charge transfer resistance represented by the first semicircle is caused by the migration of Li^+ ions through the cathode-electrolyte interface film (R_{ct1} in the equivalent circuit) on the cathode surface, whereas the

presence of a second semicircle in the mid-frequency region can be associated with the impedance caused by the movement of charged ions (Li^+) at the interface between the electrode and electrolyte solution (R_{ct2} in the equivalent circuit).[55–57] The insets of Figure 8 display an enlarged view of

Batteries & Supercaps

Research Article
doi.org/10.1002/batt.202400782

Chemistry Europe
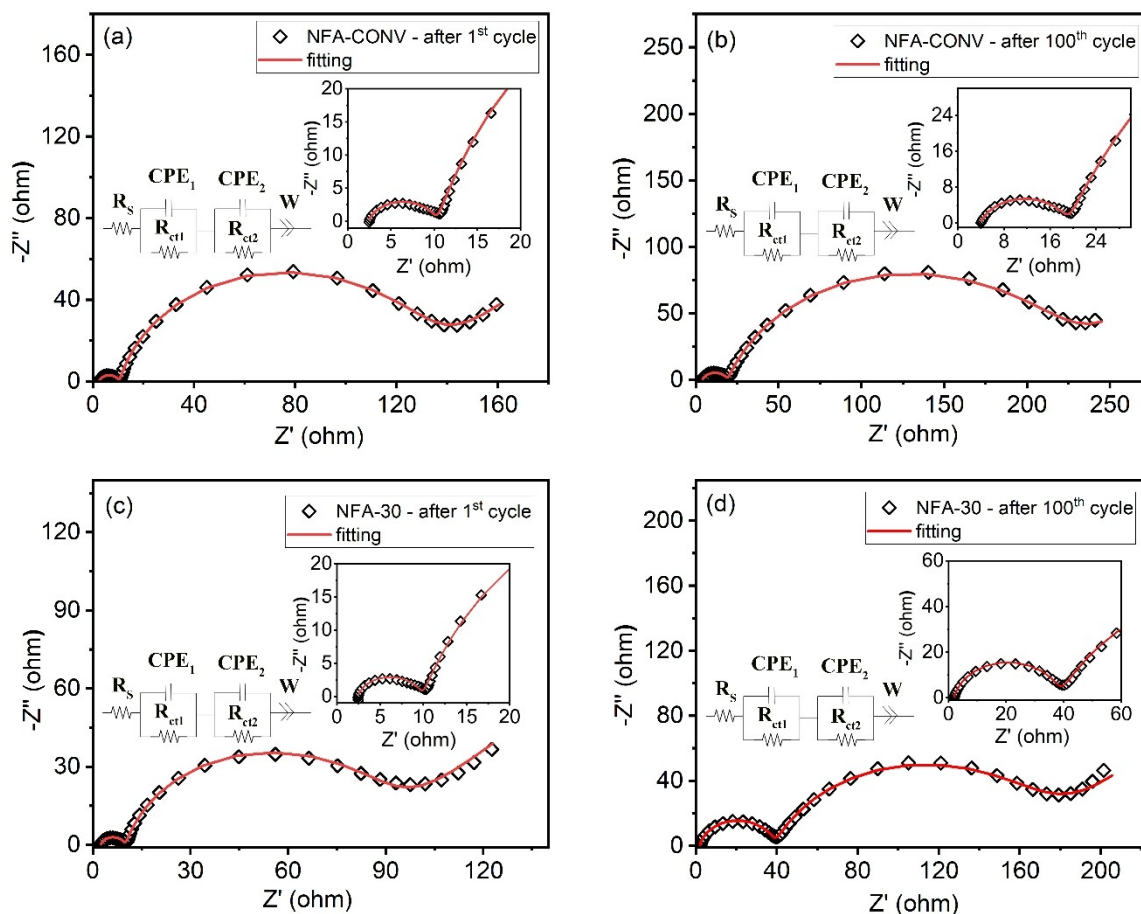European Chemical
Societies Publishing

Figure 8. Nyquist impedance plots of NFA-CONV cathode after (a) 1st cycle, and after (b) 100th cycle along with the fitted curves. Nyquist impedance plots of NFA-30 cathode after (c) 1st cycle, and after (d) 100th cycle along with the fitted curves. The equivalent circuit (containing the electrical elements) used for impedance curve fitting is given in the inset of each plot. The impedance measurement has been carried out after 1st cycle and after the 100th cycle during the long cyclic run at charged state.

the first semicircle for both Ni-rich layered oxide cathodes. The estimated impedance parameters obtained from the EIS fitting are given in Table S2. Although both electrodes exhibit nearly identical R_{ct1} after the first cycle, the NFA-30 cathode delivered about twice as much solid-electrolyte interface film resistance (R_{ct1}) as the NFA-CONV cathode after 100 charge-discharge cycles. Due to the presence of surface species (Li_2CO_3 and LiOH) on the cathode particles (as confirmed from XPS analysis) the surface of NFA-30 cathode could make thicker CEI layer after 100 charge-discharge cycle due to side reaction with organic electrolyte. Despite a severe growth of R_{ct1} for NFA-30 cathode, it still offers superior electrochemical performance than its NFA-CONV counterpart due to its higher structural stability and efficient Li^+ diffusion through the cathode electrolyte interface. The lower values of R_{ct2} for NFA-30 than NFA-CONV cathode further support its excellent electrochemical performance. Such lower charge transfer resistance can be attributed to the better structural stability of NFA-30 cathode due to less disorder in the crystal lattice and the absence of microcracks in its microstructure (See the post-SEM study in the Supplementary Information). After 100 cycles, the microstructural changes of NFA-CONV and NFA-30 cathode were investigated using XRD.

The detailed discussion and the corresponding figure (Figure S18) are providing in Supplementary Information.

The NFA-30 cathode exhibits a spherical microstructure with a size range of 4–5 µm and an average primary particle size of 500 nm, consisting of tightly packed nanoparticles. The small sizes of these primary particles offers short diffusion path lengths and a fast diffusion rate, facilitating efficient carrier migration. Additionally, the densely connected primary particles in the NFA-30 cathode enhance electronic conduction due to their interconnected nature, resulting in excellent rate capability. However, this tightly packed spherical structure may induce significant stress during continuous charge-discharge cycles, potentially leading to capacity degradation. This issue could be mitigated through doping or microstructure engineering. Despite the challenges typically associated with microspheres, the NFA-30 cathode, even without any modifications, delivers superior performance due to its structural stability. Its improved performance is further supported by its microstructural retention capability without the generation of microcracks (Figure S19), reduced surface reconstruction caused by cationic disorder, as indicated by the surface composition, which shows

Batteries & Supercaps

Research Article
doi.org/10.1002/batt.202400782

Chemistry
Europe

European Chemical
Societies Publishing

a higher Ni^{3+} to Ni^{2+} ratio, suggesting a lower abundance of the NiO rock-salt phase (as explained in the XPS section).

Although a significant amount of residual lithium species is present on the surface, which may have slightly affected capacity retention at all C-rates, the NFA-30 cathode still outperforms the conventionally annealed cathode. This demonstrates that the NFA-30 cathode exhibits superior performance even without additional material modifications. The exceptional performance of the NFA-30 cathode can be further enhanced through the integration of mitigation techniques.

Numerous approaches have been proposed in the literature thus far to improve Ni-rich layered oxide's electrochemical properties.[58–61] Several procedures have been thoroughly investigated for Ni-rich layered oxide, including doping, coating, electrolyte alteration, and microstructural tuning (single crystal synthesis, synthesis of distinct morphology, and synthesis of concentration gradient structure). Although different synthesis routes and the tuning of synthesis parameters are well-studied in the literature for Ni-rich cathode,[12] the tuning of annealing parameters is less explored. Here we demonstrate that, in the absence of any other material modification like surface coatings or substitutions, the electrochemical properties in the Ni-rich layered oxide system can be enhanced by replacing conventional annealing in tubular furnace with Microwave annealing. The process is of interest for creating next-generation lithium-ion batteries since it has several benefits over conventional annealing, such as increased reaction speed and efficiency,[17] lower energy consumption, and higher structural quality.

To compare the electrochemical performance of MW-treated Co-free NFA cathode with similar Co-containing or Co-free Ni-rich layered oxide cathode (Nickel percentage-90%) synthesized by other methods (annealed in conventional furnace) reported in the literature, a comparison table is provided in the supplementary information (Table S3). It is noteworthy that the Co-free $LiNi_{0.9}Fe_{0.05}Al_{0.05}O_2$ cathode produced by MW sintering in this study shows nearly identical electrochemical characteristics compared to other Co-containing or Co-free Ni-rich cathodes with a nickel percentage of 90% reported in the literature. The $LiNi_{0.9}Fe_{0.05}Al_{0.05}O_2$ cathode produced from MW demonstrated excellent rate capability, supporting the fact that replacing Co with Fe not only provides superior performance but also eliminates the other disadvantage associated with Co. We have also conducted a comparison between our study and the performance of the $LiNi_{0.9}Fe_{0.05}Al_{0.05}O_2$ cathode produced by the rheological phase reaction method. [29] Table S4 clearly shows that MW-derived $LiNi_{0.9}Fe_{0.05}Al_{0.05}O_2$ cathode shows better rate capability. However, the different electrolyte used in the two studies may account for the slightly lower capacity retention of the NFA cathode derived from MW. Comparing the electrochemical performance of the two distinct works is challenging due to the substantial influence of fabrication parameters and electrolyte specification on the electrode performance. Our study, by considering the performance of $LiNi_{0.9}Fe_{0.05}Al_{0.05}O_2$ cathodes (obtained from two different annealing protocol) carried out under identical conditions, strongly brings out the influence of MW annealing on the electrochemical performance of Ni-rich Co-free cathode.

3. Conclusions

To reduce energy consumption and CO_2 emissions during cathode manufacturing, as well as to boost reaction efficiency, Ni-rich layered oxide with the composition $LiNi_{0.9}Fe_{0.05}Al_{0.05}O_2$ is synthesized for the first time using a microwave (MW) furnace. To achieve the best optimized cathode with the best electrochemical performance, the structural and electrochemical properties of the cathode are optimized by adjusting the annealing conditions. Co-free Ni-rich $LiNi_{0.9}Fe_{0.05}Al_{0.05}O_2$ cathode obtained under optimized MW annealing conditions for 30 min (NFA-30) is compared both in terms of both structural and electrochemical properties to the cathode produced by conventional annealing (NFA-CONV). As proven by X-ray diffraction, the NFA-30 cathode displayed a more ordered layered structure than the NFA-CONV cathode. Furthermore, the morphology variation has been studied with the help of FESEM imaging. Cathode made from MW annealing exhibits better electrochemical performance. Detailed C-rate dependent rate-capability studies reveal that at any given C-rate, NFA-30 exhibits higher discharge capacity than NFA-CONV cathode. NFA-30 cathodes worked efficiently at high C-rate, showing 117.4 mAh g^{-1} at 15 C-rate, and 78.1 mAh g^{-1} at 30 C-rate. The MW-derived Ni-rich cathode materials also exhibit good cyclic stability compared to NFA-CONV cathode, due to its structural stability. The present study shows that by modifying the synthesis conditions, the microwave annealing process may be used to create Ni-rich layered oxide cathodes with good electrochemical characteristics. The growing demand of future LIB for electric vehicle application makes MW annealing more suitable in developing high energy density electrode material in much shorter time unlike conventional annealing which involve long reaction time.

4. Supplementary Information

XRD pattern of ternary precursor; Refined XRD patterns of all the cathodes; FESEM images of the precursor which have undergone pre-annealing; Low magnification FESEM images of NFA-CONV and MW-treated cathodes; EDS spectra of Ni-rich layered oxide cathodes; Table containing the estimated concentration of TM ions from EDS analysis; Elemental mapping of NFA-15, NFA-45 and NFA-60 cathode; 1st cycle charge-discharge profile of all the cathodes; CV profile of MW-treated cathodes; Table containing the impedance values of cycles cathodes; Post electrochemical XRD patterns of NFA-CONV and NFA-30 cathodes; Post electrochemical SEM images of NFA-CONV and NFA-30 cathodes; Tables showing the comparison of electrochemical performance of the present study with those reported in the literature.

Acknowledgements

Conflict of Interests

The authors declare that they have no known competing financial interests or personal relationships that could have appeared to influence the work reported in this paper.

Data Availability Statement

The data that support the findings of this study are available from the corresponding author upon reasonable request.

[1] T. Z. Ang, M. Salem, M. Kamarol, H. S. Das, M. A. Nazari, N. Prabaharan, *Energy Strateg Rev.* **2022**, *43*(8), 100939. https://doi.org/10.1016/j.esr.2022.100939.

[2] Y. Mekonnen, A. Sundararajan, A. I. Sarwat, *Conf Proc* **2016**, *2016*(6), 2–7, https://doi.org/10.1109/SECON.2016.7506639.

[3] P. Roy, S. K. Srivastava, *J. Mater. Chem. A* **2015**, *3*(6), 2454–84, https://doi.org/10.1039/C4TA04980B.

[4] M. Gutsch, J. Leker, *Appl. Energy* **2024**, *353*, 122132, https://doi.org/10.1016/j.apenergy.2023.122132.

[5] X. Wang, Y. L. Ding, Y. P. Deng, Z. Chen, Ni-Rich/Co-Poor Layered Cathode for Automotive Li-Ion Batteries: Promises and Challenges. Vol. 10, Advanced Energy Materials. Wiley-VCH Verlag; 2020, https://doi.org/10.1002/aenm.201903864.

[6] C. M. Julien, A. Mauger, *Energies* **2020** *13*(23), 6363, https://doi.org/10.3390/en13236363.

[7] C. Liao, F. Li, J. Liu, *Nanomaterials.* **2022**, *12*(11), https://doi.org/10.3390/nano12111888.

[8] G. L. Xu, X. Liu, A. Daali, R. Amine, Z. Chen, K. Amine, Challenges and Strategies to Advance High-Energy Nickel-Rich Layered Lithium Transition Metal Oxide Cathodes for Harsh Operation. Vol. 30, Advanced Functional Materials. Wiley-VCH Verlag; 2020.

[9] Z. Ahaliabadeh, X. Kong, E. Fedorovskaya, T. Kallio, *J. Power Sources* **2022**, *540*(1), 231633, https://doi.org/10.1016/j.jpowsour.2022.231633.

[10] H. Lv, C. Li, Z. Zhao, B. Wu, D. Mu, A review: Modification strategies of nickel-rich layer structure cathode (Ni ≥ 0.8) materials for lithium ion power batteries. Vol. 60, Journal of Energy Chemistry. Elsevier B. V.; 2021. p. 435–50.

[11] X. Tan, M. Zhang, J. Li, D. Zhang, Y. Yan, Z. Li, *Recent progress in coatings and methods of Ni-rich LiNi0.8Co0.1Mn0.1O2 cathode materials: A short review.* Vol. 46, Ceramics International. Elsevier Ltd, **2020**. p. 21888–901.

[12] F. I. Saaid, M. F. Kasim, T. Winie, K. A. Elong, A. Azahidi, N. D. Basri, et al., *Heliyon.* **2024**;*10*(1), e23968, https://doi.org/10.1016/j.heliyon.2023.e23968.

[13] J. Li, W. Zhong, Q. Deng, Q. Zhang, C. Yang, *Int J Extrem Manuf.* **2022**, *4*(4), https://doi.org 10.1088/2631-7990/ac92ef.

[14] J. H. Shim, C. Y. Kim, S. W. Cho, A. Missiul, J. K. Kim, Y. J. Ahn, et al., *Electrochim. Acta* **2014**, *138*, 15–21, https://doi.org/10.1016/j.electacta.2014.06.079.

[15] V. Pimenta, M. Sathiya, D. Batuk, A. M. Abakumov, D. Giaumem, S. Cassaignon, et al., *Chem. Mater.* **2017**, *29*(23), 9923–36.

[16] Z. Wang, C. Yu, H. Huang, W. Guo, J. Yu, J. Qiu, *Nano Energy.* **2021**, *85*(1), 106027, https://doi.org/10.1016/j.nanoen.2021.106027.

[17] C. Gabriel, S. Gabriel, E. H. Grant, B. S. J. Halstead, P. Michael, D. Mingos, *Chem. Soc. Rev.* **1998**, *27*(3), 213–23, https://doi.org/10.1039/A827213Z.

[18] M. R. D. Bomio, P. Lavela, A. A. G. Santiago, F. V. Motta, J. L. Tirado, *Ceram. Int.* **2023**, *49*(8), 12452–61, https://doi.org/10.1016/j.ceramint.2022.12.105.

[19] S. Shi, S, Zhang, Z. Wu, T. Wang, J. Zong, M. Zhao, et al., *J. Power Sources* **2017**, *337*, 82–91, https://doi.org/10.1016/j.jpowsour.2016.10.107.

[20] X. Wang, H. D. Pham, C. Padwal, et al., *Adv Energy Sustainability Res.* **2023**, *5*, 2300199, https://doi.org/10.1002/aesr.202300199.

[21] X. Meng, J. Wang, L. Li, *Molecules* **2023**, *28*(10), 4007, https://doi.org/10.3390/molecules28104007.

[22] S. Aryal, J. L. Durham, A. L. Lipson, K. Z. Pupek, O. Kahvecioglu, *Electrochim. Acta* **2021**, *391*, 138929, https://doi.org/10.1016/j.electacta.2021.138929.

[23] S. Lee, A. Manthiram, *ACS Energy Lett.* **2022**. 3058–63, https://doi.org/10.1021/acsenergylett.2c01553.

[24] H. Zhao, W. Y. A. Lam, L. Sheng, L. Wang, P. Bai, Y. Yang, et al., *Adv. Energy Mater.* **2022**, *12*(16), 1–36, https://doi.org/10.1002/aenm.202103894.

[25] J. Wang, Z. Cui, C. Wang, Y. Liu, Y. Chen, *Solid State Ionics.* **2022**, *379*(4), 115912, https://doi.org/10.1016/j.ssi.2022.115912.

[26] A. Celeste, M. Paolacci, P. G. Schiavi, S. Brutti, M. A. Navarra, L. Silvestri, *ChemElectroChem.* **2023**, *10*(5), https://doi.org/10.1002/celc.202201072.

[27] B. C. Jang, J. T. Son, *J Nanosci Nanotechnol.* **2016**, *16*(10), 10649–53, https://doi.org/10.1166/jnn.2016.13212.

[28] N. Muralidharan, R. Essehli, R. P. Hermann, A. Parejiya, R. Amin, Y. Bai, et al., *J Power Sources.* **2020**, *471*(3), 228389, https://doi.org/10.1016/j.jpowsour.2020.228389.

[29] R. Sun, Y. Guo, Y. Chen, N. Gao, H. Li, Q. Liu, et al., *Mater. Lett.* **2023**, *342*(3), 134307, https://doi.org/10.1016/j.matlet.2023.134307.

[30] E. Elmaataouy, A. Chari, A. El Bendali, M. Tayoury, R. Amine, M. Aqil, et al., *Batteries.* **2023**, *9*(1), https://doi.org/10.3390/batteries9010023.

[31] X. Guo, S. Greenbaum, F. Ronci, B. Scrosati, *Solid State Ionics.* **2004**, *168*(1–2), 37–49.

[32] R. Guo, B. M. Gallant, *Chem. Mater.* **2020**, *32*(13), 5525–33, https://doi.org/10.1021/acs.chemmater.0c00333.

[33] K. H. Choi, X. Liu, X. Ding, Q. Li, *Ionics* **2020**, *26*(3), 1063–80, https://doi.org/10.1007/s11581-019-03429-z.

[34] W. Liu, P. Oh, X. Liu, M J. Lee, W. Cho, S. Chae, et al., *Angew. Chem. Int. Ed.* **2015**, *54*(15), 4440–57.

[35] C H. Jung, D. H. Kim, D. Eum, K. H. Kim, J. Choi, J. Lee, et al., *Adv. Funct. Mater.* **2021**, *2010095*, 1–12, https://doi.org/10.1002/adfm.202010095.

[36] C. Material, *Vibrational Spectroscopy and Electrochemical Properties Lithium Batteries E'* **1997**, *3*, 170–6. https://doi.org/10.1007/BF02375613.

[37] C. M. Julien, A. Mauger, *AIMS Press* **2018**, 650–98, https://doi.org/10.3934/matersci.2018.4.650.

[38] S. Mitra, C. Sudakar, *Battery Energy* **2024**, *2*, 20230066, https://doi.org/10.1002/bte2.20230066.

[39] E. Flores, P. Novák, E. J. Berg, *Front Energy Res.* **2018**, *6*(82), https://doi.org/10.3389/fenrg.2018.00082.

[40] M. Heber, K. Hofmann, C. Hess, *Batteries.* **2022**, *8*(2), 10, https://doi.org/10.3390/batteries8020010.

[41] S. Tanaka, M. Taniguchi, H. Tanigawa, *J. Nucl. Mater.* **2000**, *283–287*(2), 1405–8, https://doi.org/10.1016/S0022-3115(00)00251-8.

[42] K. N. Wood, G. Teeter, *ACS Appl. Energ. Mater.* **2018**, *1*(9), 4493–504.

[43] R. Zhao, Z. Yang, J. Liang, D. Lu, C. Liang, X. Guan, et al., *J. Alloys Compd.* **2016**, *689*, 318–25, DOI 10.1016/j.jallcom.2016.07.230.

[44] A. M. Andersson, D. P. Abraham, R. Haasch, S. MacLaren, J. Liu, K. Amine, *J. Electrochem. Soc.* **2002**, *149*(10), A1358, DOI 10.1149/1.1505636.

[45] N. Andreu, D. Flahaut, R. Dedryvère, M. Minvielle, D. Gonbeau, *ACS Appl. Mater. Interfaces* **2015**, *7*(12), 6629–6636, https://doi.org/10.1021/am5089764.

[46] W. Xin, Z. Xiaoyu, C. Fangyuan, W. Peng, L. Qi, .X. Jia, L. Qing, X. Yue, S. Shixiong, F. Chun, H. Jiantao, *J. Mater. Chem. A* **2022**, 16666–16674, https://doi.org/10.1039/d2ta02472a.

[47] O. Bondarchuk, A. P. LaGrow, A. Kvasha, T. Thieu, E. Ayerbe, I. Urdampilleta, *Appl. Surf. Sci.* **2021**, *535*(6), 147699, https://doi.org/10.1016/j.apsusc.2020.147699.

[48] M. Akhilash, P. S. Salini, B. John, T D. Mercy, *J. Alloys Compd.* **2021**, *869*, 159239, https://doi.org/10.1016/j.jallcom.2021.159239.

[49] J. Xu, F. Lin, M. M. Doeff, W. Tong, *J. Mater. Chem. A* **2017**, *5*(3), 874–901, https://doi.org/10.1039/C6TA07991A.

[50] N. Y. Kim, T. Yim, J. H. Song, J. S. Yu, Z. Lee, *J. Power Sources* **2016**, *307*, 641–8.

[51] S. Jamil, G. Wang, L. Yang, X. Xie, S. Cao, H. Liu, et al., *J Mater Chem A.* **2020**, *8*(40), 21306–16, https://doi.org/10.1039/D0TA07965K.

[52] S. Wu, X. Zhang, S. Ma, E. Fan, J. Lin, R. Chen, et al., *Small.* **2022**, *18*(47), 1–9, https://doi.org/10.1002/smll.202204613.

[53] A. Van Der Ven, J. Bhattacharya, A. A. Belak, *Acc. Chem. Res.* **2013**, *46*(5), 1216–25, https://doi.org/10.1021/ar200329r.

[54] U. Tröltzsch, O. Kanoun, H. R. Tränkler, *Electrochim. Acta* **2006**, *51*(8–9), 1664–72, https://doi.org/10.1016/j.electacta.2005.02.148.

[55] M. Viji, P. Swain, P. S. V. Mocherla, C. Sudakar, *RSC Adv.* **2016**, *6*(46), 39710–7, https://doi.org/10.1039/C6RA04468A.

[56] J. P. Schmidt, T. Chrobak, M. Ender, J. Illig, D. Klotz, E. Ivers-Tiffée, *J. Power Sources* **2011**, *196*(12), 5342–8, https://doi.org/10.1016/j.jpowsour.2010.09.121.

[57] Y. C. Li, W. M. Zhao, W. Xiang, Z. G. Wu, Z. G. Yang, C. L. Xu, et al., *J. Alloys Compd.* **2018**, *766*, 546–55.

[58] W. Yan, S. Yang, Y. Huang, Y. Yang, Y. Guohui, *J. Alloys Compd.* **2020**, *819*, 153048, https://doi.org/10.1016/j.jallcom.2019.153048.

[59] K. Zou, W. Deng, D. S. Silvester, G. Zou, H. Hou, C. E. Banks, et al., *ACS Nano.* **2024**, *18*(31), 19950–20000.

[60] K. Zou, M. Jiang, T. Ning, L. Tan, J. Zheng, J. Wang, et al., *J. Energy Chem.* **2024**, *97*, 321–31. Available from: https://doi.org/10.1016/j.jechem.2024.05.053.

[61] M. Jiang, P. Wang, Q. Chen, Y. Zhang, Q. Wu, L. Tan, et al., *Chin. Chem. Lett.* **2024**, 110040 https://doi.org/10.1016/j.cclet.2024.110040.